Review of Advances in Quantitative Eddy Current Nondestructive Evaluation

B. A. Auld[1] and J. C. Moulder[2]

A comprehensive review of advancements in eddy current (EC) modeling is presented. This paper contains three main sections: a general treatise of EC theory, the thin skin EC forward modeling, and the EC inverse problem. (1) The general treatise of eddy current theory begins with an exposition of the reciprocity formulas for evaluating probe impedance changes, which are derivable from first principles. Two versions of the reciprocity formulas, one with a surface integral and the other with a volume integral, are given. Any particular type of defect, as well as both one-port and two-port probes, can be treated. Second, a brief account of analytical and numerical methods for calculating the field distributions is presented. Third, theory of probe/material interactions with various defect types is described. (2) The paper then proceeds to the forward modeling section, which contains a detailed treatment of the eddy current forward problem for surface breaking cracks and EDM notches in the thin skin approximation. (3) The inverse problem section begins with a general review of commonly used inversion methods, exemplified by selected references from the literature, followed by more detailed examinations of EC inversions for surface breaking cracks and slots. The last part of this section is devoted to the inverse problem for layered structures. Although being a review in nature, the paper contains a number of new accounts for time-domain eddy current interactions. In particular, a modification is proposed to the reciprocity formula in order to take a better account of pulsed eddy current signals.

KEY WORDS: Eddy current modeling; quantitative NDE; reciprocity formulas; thin skin theory; eddy current inversion; pulsed eddy current.

1. INTRODUCTION

The original development of eddy current probes for defect detection and material characterization was based on circuit concepts. In this approach, the metallic testpiece was pictured as the short-circuited secondary of a transformer, with the probe coil constituting the primary. This model was formalized by an equivalent circuit diagram, in which a series resistance in the primary represented coil losses and a series resistance in the secondary represented resistive losses in the testpiece. The induction of eddy currents in the testpiece was characterized by the lumped mutual inductance of the transformer, which was taken to vary inversely with the distance between the probe and the metal surface (liftoff distance) according to some empirical law. A defect in the metal was considered to alter the series resistance in the secondary of the transformer, by an amount depending on the size of the defect and its position relative to the probe coil. Similarly, global changes in the resistivity of the metal and resistive inhomogeneities, etc., were also considered as changes in the secondary resistance.

The circuit model qualitatively predicted the general behavior of changes in the probe input impedance due to the presence of a defect and variations of the liftoff

[1] E. L. Ginzton Laboratory, Stanford University, Stanford, California 94305.
[2] Center for Nondestructive Evaluation, Iowa State University, Ames, Iowa 50011.

distance. It showed, for example, that the probe impedance change ΔZ has a different phase angle for a defect and for a liftoff variation. But it could not provide quantitative information about the defect and liftoff signals, or about the effect on these signals of changes in the defect and probe geometries. The first step beyond this concept was taken by Burrows,[1] who first introduced the use of reciprocity in eddy current probe analysis. His method (for defects in the form of small ellipsoidal inclusions with altered resistive and magnetic properties) first calculated the magnetic moment of the inclusion induced through its interaction with the eddy current and magnetic field distributions excited in the metal testpiece by a fixed input current I injected at the probe terminals. The reaction of the defect back on the probe was then evaluated by finding the voltage change ΔV at the probe terminals, created by the altered flux linkages originating from the induced magnetic moment of the inclusion. Reciprocity arguments were used to simplify the analysis. Combining the fixed input current I and the voltage change ΔV due to the presence of the defect provided an expression for the probe impedance change ΔZ due to the defect. The defect's geometry was also included in the analysis, through the dependence of its induced moment on the shape of the inclusion.

Burrows' analysis, which was applied to both single-coil (one-port) and drive-coil/pickup-coil (two-port) probe geometries, was an important advance in eddy current probe modeling. It introduced explicitly the dependence of the defect signal on the field distribution of the probe and therefore on the probe geometry, showing that quantitative characterization of a defect could be achieved only if the probe field itself was accurately known. But the model had shortcomings. It applied rigorously only to ellipsoidal defects, and then only if the defect was so small that it lay in an essentially uniform region of the probe field. These difficulties can be overcome by treating the probe/defect interaction as an electromagnetic field problem rather than a circuit problem. This approach, to be presented here in detail, strongly resembles the analysis used in microwave theory to obtain equivalent circuit representations for a distributed field structure.[2,13] But, in the present case, the method is applied to quasistatic fields of kilohertz frequencies, rather than to propagating fields at gigaherz frequencies.

Current applications of eddy current probes include the detection and characterization of

- surface-breaking and internal cracks;
- pits, internal voids, and inclusions;
- nonlocalized material inhomogeneities, as in corrosion problems;

- variations in the properties of homogeneous metals due, for example, to processing errors occuring during manufacture; and
- variation in the thickness and material properties of surface coatings.

For all of the listed defects, having a model that accurately predicts the ΔZ of the probe is a prerequisite to the satisfactory performance of eddy current diagnostics. First, such a model should provide a solution to the forward problem—that is, a quantitative analysis of probe response to defects of all types. Second, the model should be formulated so as to facilitate the development of solutions to the inverse problem—that is, the quantitative characterization of a particular defect from measurements of changes in the eddy current probe impedance as the probe is scanned over the defect. Finally, a satisfactory model should also accurately predict probe impedance changes due to the liftoff and tilt variation as the probe is scanned over a metal surface. The background "clutter" arising from liftoff and tilt variations constitutes the primary limitation on the effective signal-to-noise of a defect signal.

The body of the paper begins, in Section 2.1, with the development from first principles of relations for the change in impedance ΔZ of an eddy current probe in the presence of a defect. General formulas are obtained without restriction to any particular type of defect, for both one-port and two-port probes. The results are stated in two alternative forms: (i) as a field integral over a surface enclosing the defect and (ii) as a field integral over the volume of the defect. These integrals involve the probe field distribution in the absence and in the presence of the defect, as well as the dimensions and shape of the defect. To evaluate accurately a defect signal ΔZ, it is necessary to begin with a model for the probe field in the absence of a defect. Section 2.2 presents a brief overview of analytical and numerical methods used for calculating the field distributions of both air-core and ferrite-core probes over a metal surface. Then, finally, Section 2.3 considers probe/material interactions for the various types of defects listed above. After this general treatment, Sections 3 continues with a detailed treatment in the thin skin approximation of the eddy current forward problem for surface-breaking cracks and EDM notches. Section 4 begins with a general review of commonly used inversion methods, exemplified by selected references from the literature. Section 4.2 then examines in more detail the inversion of eddy current signals from surface-breaking cracks and slots, while Section 4.3 treats the inversion problem for layered structures. In both cases examples are given of new developments in the use of pulsed eddy current instruments.

2. GENERAL ELECTROMAGNETIC FIELD MODELING

2.1. ΔZ Relations

The traditional approach to probe modeling used an equivalent circuit model to provide a qualitative description of probe performance.[4] Burrows later developed a quantitative equivalent circuit model, for defects consisting of small ellipsoidal inclusions and voids.[1] His approach was based on use of the electromagnetic field reciprocity relation (Lorentz) to establish a circuit reciprocity relation for two-port probes. Change in the coupling between the drive coil and the pickup coil, due to the presence of a defect, was formulated using polarizations of the defect induced by exciting the drive and pickup coils in turn. Applying the circuit reciprocity relation then yielded the quantitative change ΔZ_{21} in mutual impedance between the two coils.

Later applications of the Lorentz reciprocity relation to probe modeling were based on the concepts of microwave circuit theory.[2,3] This approach was followed by Bahr[5] to analyze 100-GHz eddy current detection in a two-port waveguide driven system, by Auld[6] for a one-port microwave ferrite resonator probe, and by Zaman et al.[7] for a one-port coil probe. In all of these papers, exact expressions give ΔZ for arbitrary defects in terms of the probe fields in the absence and in the presence of the defect. Reference 5 expresses ΔZ in the form of a surface integral, while Refs. 6 and 7 give both volume and surface integral forms. These results generalize Burrows' work and define the electromagnetic boundary value problems that must be solved to evaluate ΔZ. The three references cited all begin with an integration of the Lorentz reciprocity relation over the domain of the problem and arrive at impedance relations by manipulating this integral. In the following development, a more physical approach is presented. Probe impedances for the unflawed and flawed states are first expressed in terms of Poynting-type field integrals, and the difference ΔZ of these impedances is subsequently related to either a surface integral or a volume integral over the region of the defect.

2.1.1. One-Port Probes

To illustrate the field-analytic approach, the one-port probe geometry in Fig. 1 is chosen as a first example. In complex notation, the time-harmonic voltage and current at the probe terminals are
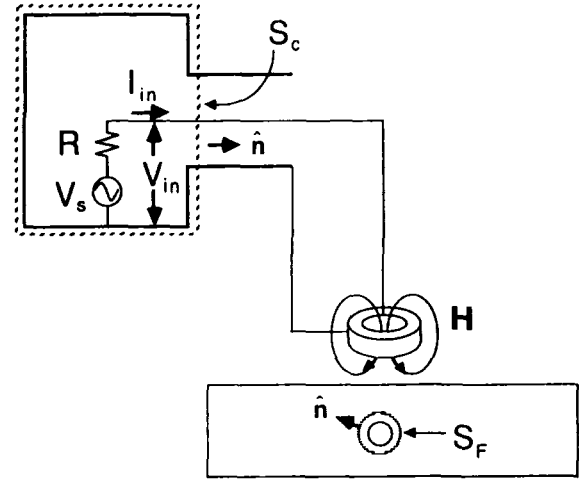

Fig. 1. General one-port (or absolute) probe geometry with a coaxial line feed.

$$V_{IN}(t) = \text{Re } Ve^{i\omega t} \tag{1a}$$

$$I_{IN}(t) = \text{Re} Ie^{i\omega t} \tag{1b}$$

and the input impedance is

$$Z = \frac{V}{I} \tag{2}$$

The basic probe field/impedance relationship can be established using Poynting's theorem. Complex power delivered at the input terminal plane in Fig. 1 is defined as

$$P_{IN} = \frac{VI^*}{2} = \frac{ZII^*}{2} \tag{3a}$$

From Poynting's theorem, this is also given as

$$P_{IN} = \frac{1}{2} \int_{S_c} \vec{E} \times \vec{H}^* \cdot \vec{n} dS \tag{3b}$$

where $\vec{E}$ and $\vec{H}$ are the probe fields corresponding to V and I in 3(a) and S_c is the area of the coaxial line section at the terminal plane.

Because the impedance of a circuit is independent of the excitation phase, the input current at the terminal plane can, without loss of generality, be taken to have zero phase, so that I is pure real and the conjugate sign can be dropped in (3a). Since the magnetic field $\vec{H}$ of the coaxial line mode has the same phase as I at any particular cross section, the complex conjugate can also be dropped in (3b). Then from (3a) and (3b),

$$Z_a = \frac{2P_{IN}}{I_a^2} = \frac{1}{I_a^2} \int_{S_c} \vec{E}_a \times \vec{H}_a \cdot \vec{n} dS \tag{4a}$$

The impedance in (4a) is defined to be the probe impedance in the absence of a defect, where $\vec{E}_a$ and $\vec{H}_a$ are the probe fields excited in the unflawed testpiece by the probe terminal current I_a. In the presence of a defect the probe impedance is

$$Z_b = \frac{1}{I_b^2} \int_{S_c} \vec{E}_b \times \vec{H}_b \cdot \vec{n} dS \qquad (4b)$$

where $\vec{E}_b$ and $\vec{H}_b$ are the probe fields excited in the presence of a defect by the probe terminal current I_b. Since the input impedance at the terminal is independent of the drive current, the condition

$$I_b = I_a = I$$

can always be imposed in (4a) and (4b). The change in probe impedance due to the defect is then, subtracting (4a) from (4b), given as

$$\Delta Z = Z_b - Z_a$$
$$= \frac{1}{I^2} \int_{S_c} (\vec{E}_b \times \vec{H}_b - \vec{E}_a \times \vec{H}_a) \cdot \vec{n} dS \qquad (5)$$

Because the $\vec{H}$ field at S_c is proportional to the input current, it follows from

$$I_a = I_b \qquad (6a)$$

that

$$\vec{H}_a = \vec{H}_b \qquad (6b)$$

on S_c. Consequently, in (5) the subscripts to H can be interchanged between the first term under the integral and the second, yielding

$$\Delta Z = \frac{1}{I^2} \int_{S_c} (\vec{E}_b \times \vec{H}_a - \vec{E}_a \times \vec{H}_b) \cdot \vec{n} dS \qquad (7)$$

The expression for ΔZ in (7) can now be converted to a field integral over the defect by invoking the Lorenz reciprocity relation [3]

$$\vec{\nabla} \cdot (\vec{E}_b \times \vec{H}_a - \vec{E}_a \times \vec{H}_b) = 0 \qquad (8a)$$

between arbitrary solutions to Maxwell's equation in a source-free region with fixed material properties, where the a and b solutions are the fields defined in (4a) and (4b). In particular, (8a) applies to the fields defined in (4) at all points in the region exterior to the source and the defect in Fig. 1—that is, at all points outside the surfaces S_c and S_F in Fig. 1. If this region is enclosed by a spherical surface of radius R and (8a) is integrated over the volume bounded by the total surface S comprising the enclosing sphere plus the surfaces around the source

and the defect (Fig. 1), use of the divergence theorem converts the result to the surface integral form

$$\oint_S (\vec{E}_b \times \vec{H}_a - \vec{E}_a \times \vec{H}_b) \cdot \vec{n} dS = 0 \qquad (8b)$$

where $\vec{n}$ is defined in Fig. 1 as the *inward* normal to the entire boundary surface S. The contribution from the enclosing sphere vanishes as $R \rightarrow \infty$ (Appendix A),[8] and the integral around the source reduces to an integral over the coaxial cross section S_c, if the shielding around the source is assumed perfectly conducting. There results, then,

$$\int_{S_c} (\vec{E}_b \times \vec{H}_a - \vec{E}_a \times \vec{H}_b) \cdot \vec{n} dS =$$
$$-\int_{S_F} (\vec{E}_b \times \vec{H}_a - \vec{E}_a \times \vec{H}_b) \cdot \vec{n} dS \qquad (9)$$

where S_F is *any* surface enclosing the defect (Fig.1). (The most convenient definition of S_F depends on the geometry of the defect, as shown below.) Substitution of this result into (7) gives an expression for ΔZ in terms of an integral around the defect,

$$\Delta Z = \frac{1}{I^2} \int_{S_F} (\vec{E}_a \times \vec{H}_b - \vec{E}_b \times \vec{H}_a) \cdot \vec{n} dS \qquad (10a)$$

where the minus sign in (9) has been suppressed by reversing the order of the cross products. Recall that subscript a defines fields in the absence of the defect and subscript b defines fields in the presence of the defect.

Appendix B shows how this result can be converted to a volume integral format,

$$\Delta Z = \frac{i\omega}{I^2} \int_{V_F} (\vec{H}_a \cdot [\delta\mu \cdot \vec{H}_b]$$
$$- \vec{E}_a \cdot [\delta\varepsilon \cdot \vec{E}_b]) dV \qquad (10b)$$

where V_F is the volume of the flaw and $\delta\varepsilon$ and $\delta\mu$ are the differences of permittivity and permeability between the flawed "b" and the unflawed "a" states of the testpiece. Both the permittivity and the permeability are complex. In the normal range of frequencies for eddy current testing, displacement currents in metal testpieces are negligible compared with conduction currents and the approximation

$$\varepsilon + \frac{\sigma}{i\omega} \cong \frac{\sigma}{i\omega} \qquad (11)$$

can be made. Equation (10b) generalizes Burrows' analysis to completely arbitrary geometries. It should be emphasized that no approximations have been made in the above derivation.

There are no restrictions on the anisotropy and inhomogeneity of ε and μ, nor are there any restrictions on the shape of the defect. Choice between the surface integral format (10a) and the volume integral format (10b) depends on the type of defect involved and on the analytic approximations or numerical methods used in evaluating the b-subscripted fields under the integrals. Note that the surface S_F in Fig. 1 can be chosen arbitrarily, as long as it encloses the defect. This flexibility of choice may often be used to simplify calculation of ΔZ.

2.1.2. Two-Port Probes

The analysis presented above applies to the one-port (or absolute) probe illustrated in Fig. 2a and to any of the various absolute probe geometries used in practice: coil axis horizontal,[9,10] ferrite core,[11,12] rectangular-shaped coil with rounded corners and horizontal axis,[13] nonrectangular winding cross section,[14] uniform field ferrite core,[15,16] encircling coil,[17] pull-through coil,[18] and waveguide probe.[19]

The same analysis is applicable to the differential probe illustrated in Fig. 2b. In this case, the one-port analysis is used to evaluate ΔZ separately for the left-hand and right-hand coils, and taking the difference. Alternatively, using bridge circuit electronics, the probe may be regarded as a two-port probe with the input port at the bridge excitation terminal and the output port at the bridge balance terminal.

To illustrate the formulation of ΔZ for a two-port probe, the reflection probe in Fig. 2c is taken as an example. In this case, the defect is interrogated by exciting the drive coil 1 and the presence of the defect is detected by observing a change in the transfer signal to the pickup

coil 2. In many reflection probes there is no transfer signal in the absence of a defect.

Regardless of the specific probe geometry, any two-port reflection probe can be represented schematically as shown in Fig. 3. Figure 3a is a general T-network equivalent for calculating the transfer signal. Changes in the impedances shown are to be evaluated in terms of the actual fields around the flaw using ΔZ formulas analogous to (10a) and (10b). The derivations follow the same general procedure as before. For example, to derive ΔZ_{12}, the two solutions for the Lorenz reciprocity relation in (8a) and (8b) are defined as in Figs. 3b and c, so that the counterpart of (9) is

$$\int_{S_1+S_2} (\vec{E}_b \times \vec{H}_a - \vec{E}_a \times \vec{H}_b) \cdot \vec{n} \, dS =$$

$$-\int_{S_F} (\vec{E}_b \times \vec{H}_a - \vec{E}_a \times \vec{H}_b) \cdot \vec{n} \, dS \qquad (12)$$

As in Fig. 1, the magnetic field at any terminal plane in Fig. 3 is proportional to the current at the same terminal plane. Because of the boundary conditions on the currents in Fig. 3, the left-hand side of (12) reduces to

$$\int_{S_1} (\vec{E}_b \times \vec{H}_a) \cdot \vec{n} \, dS - \int_{S_2} (\vec{E}_a \times \vec{H}_b) \cdot \vec{n} \, dS$$

$$= V_{1b}I_{1a} - V_{2a}I_{2b} \qquad (13)$$

In (13), the electric fields $\vec{E}$ and the magnetic fields $\vec{H}$, as well as the voltages V and currents I, are evaluated at the terminal planes S_1 and S_2 in Fig. 3, where only the fundamental coaxial transmission line mode is present. For this mode, the electric field has only a radial component and the magnetic field only an azimuthal component,
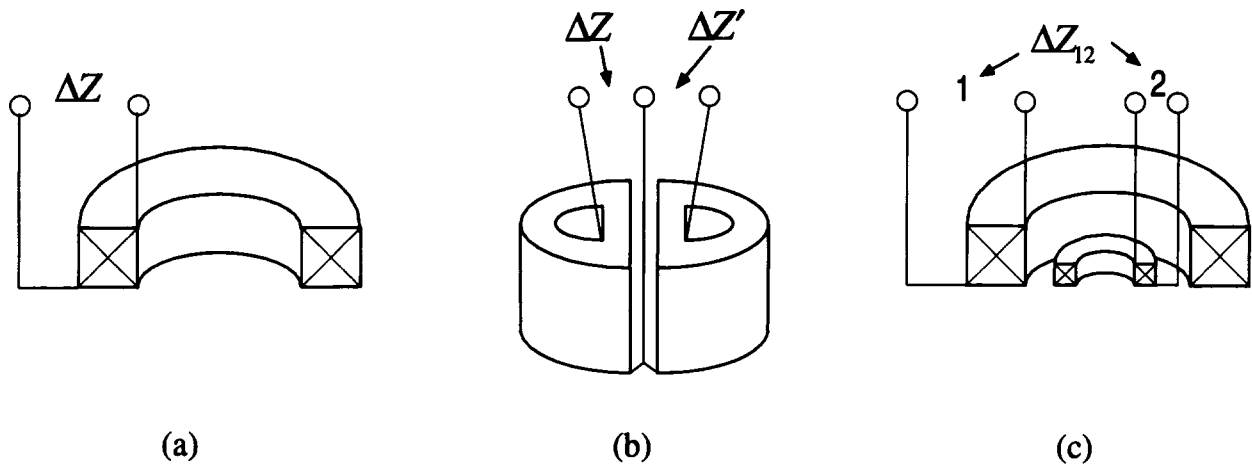

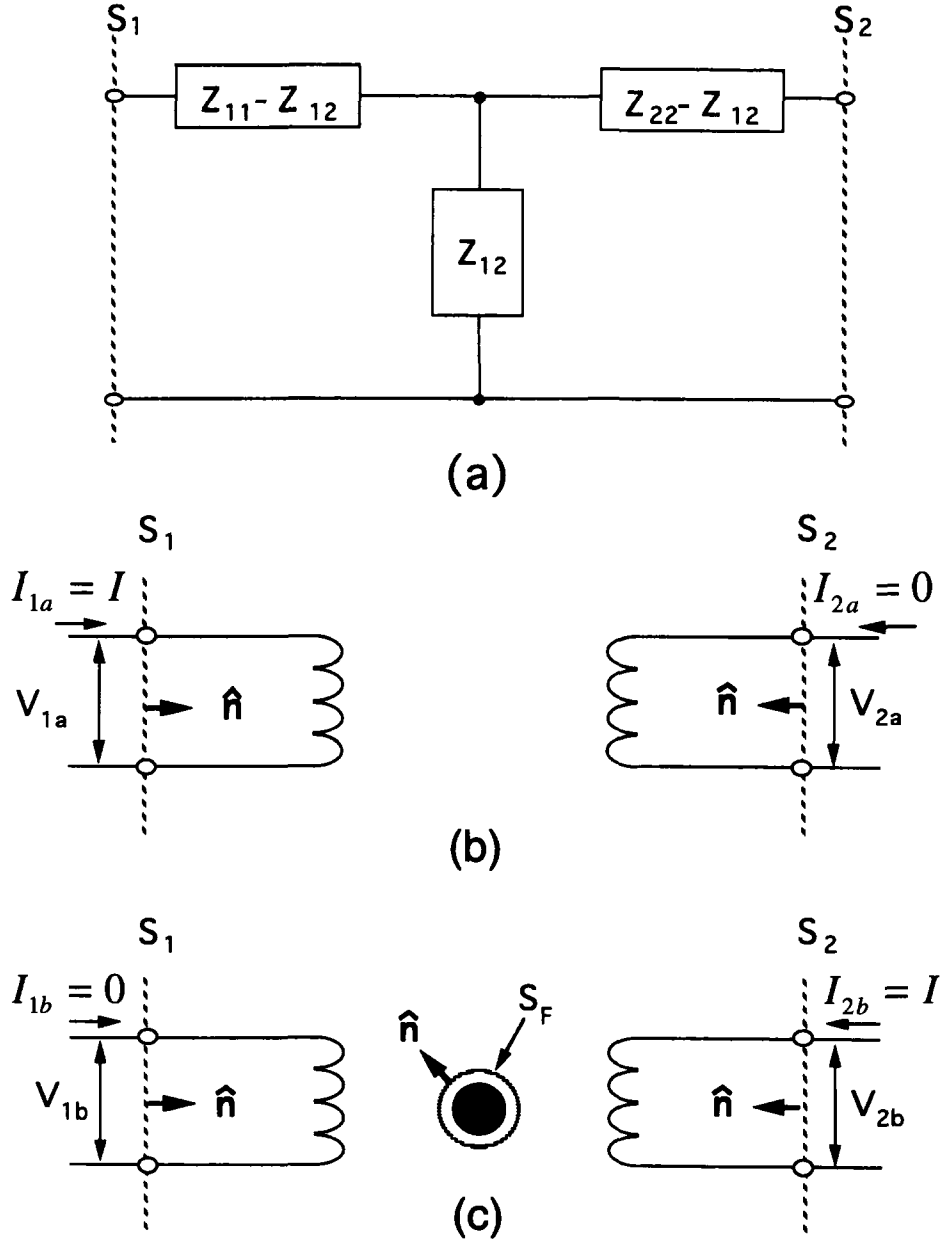**Fig. 2.** Basic types of eddy current probes.

Fig. 3. Reflection probe analysis. (a) Equivalent circuit. (b) Solution a. (c) Solution b.

both components being independent of the azimuthal coordinate ϕ and inversely proportional to the radial coordinate r.[2,3] Consequently, the cross products under the integrals on the left-hand side of (13) reduce to algebraic products of the form $E_r H_\phi$. The ϕ part of the surface integrations then introduce a multiplier 2π, which converts the magnetic field factor into the coaxial line current, while the radial part of the integration converts the electric field factor into the coaxial line voltage. This produces the voltage–current products on the right-hand side of (13).

This result is converted to a transfer impedance change by writing out the impedance matrix equations of the T-network for solutions "a" and "b" in Fig. 3. For the a-subscripted solution ($I_{1a} = I$, $I_{2a} = 0$), noting that $Z_{12} = Z_{21}$ by reciprocity,

$$V_{1a} = I_{1a}Z_{11a} + I_{2a}Z_{12a} = IZ_{11a} \qquad (14a)$$

$$V_{2a} = I_{1a}Z_{12a} + I_{2a}Z_{22a} = IZ_{12a} \qquad (14b)$$

and for the b-subscripted solution ($I_{1b} = 0$, $I_{2b} = I$)

$$V_{1b} = I_{1b}Z_{11b} + I_{2b}Z_{12b} = IZ_{12b} \qquad (15a)$$

$$V_{2b} = I_{1b}Z_{12b} + I_{2b}Z_{22b} = IZ_{22b} \qquad (15b)$$

Substitution of (15a) and (14b) into (13) and (12) yields

$$Z_{12b} - Z_{12a} = \Delta Z_{12} = \frac{1}{I^2}$$

$$\int_{S_F} (\vec{E}_a \times \vec{H}_b - \vec{E}_b \times \vec{H}_a) \cdot \vec{n} dS \qquad (16a)$$

As in the case of (10a) and (10b), the surface integral in (16a) can be converted to volume form, yielding

$$\Delta Z_{12} = \frac{i\omega}{I^2}$$

$$\int_{V_F} (\vec{H}_a \cdot [\delta\mu \cdot \vec{H}_b] - \vec{E}_a \cdot [\delta\varepsilon \cdot \vec{E}_b]) dV \qquad (16b)$$

The above formulation of ΔZ_{12} is applicable to any of the two-port probe types currently in use: differential pickup coil,[20] remote field,[21-23] encircling coils,[24-26] horizontal drive and pickup coils,[13,27,28] vertical drive and horizontal pickup coils,[29,30] geometrically anisotropic,[31] and ferrite core.[32,33] It can also be applied to the differential probe in Fig. 2b, as noted at the beginning of this subsection.

These and other ΔZ relations can also be formulated for eddy current probe arrays.[34-38] The ΔZ formulas (10a) and (10b) and(16a) and (16b) are *exact* provided that exact distributions are used for the a-field (defect absent) and the b-field (defect present). These two fields may be described in operational terms as the interrogating field a and the response field b. A number of mathematical methods have been used to model the a-field. As noted in Section 1, the accuracy of an eddy current measurement depends critically on having a precise evaluation of this field. However, having a correct field analysis for an ideal probe is not sufficient to ensure accurate signal prediction. In an actual probe, small artifacts in probe construction are known to induce very significant changes in the a-field, and techniques have been devised to measure the a-field distribution directly. These questions are addressed in Section 2.2.3. Determination of the b-field is considerably more complicated. But it is seen from the ΔZ formulas that this field is needed only in the near-vicinity of the defect, a feature that lends itself to the use of approximations and simplifies numerical evaluation of ΔZ.

Section 2.2 reviews in general terms the various methods, analytic and numerical, currently used in evaluating the a-field (unflawed testpiece). Modeling of the b-field (flawed testpiece) is considered in Section 2.3. A

general review of b-field modeling is given for the various types of defects listed in Section 1, with particular emphasis on cracks. Section 3 continues with a detailed treatment of surface-breaking cracks and EDM notches.

2.2. Probe Field Modeling

2.2.1. Air Core Coils

A classical study of circular air core coils over a metal surface is given in an analytical formulation by Dodd and Deeds, first performed for a single circular coil over various planar structures and for a single encircling coil over uncladded and cladded cylinders.[39] An essential feature of the Dodd and Deed analysis at typical eddy current frequencies is that the actual current distribution in the wire cross section is approximated by a current filament. This method was later extended to multilayer cylinders[40] and to circular drive/pickup assemblies. [41] The approach is based on use of the vector potential, $\vec{A}$, which, for the axisymmetric structures considered, has only an azimuthal component.

The a-field for an absolute probe (Fig. 2a) is calculated in terms of the current I in the coil by constructing the vector potentials in the air medium and in the metal, and imposing continuity at the interface. Solution of any electromagnetic problem is simplified if the dimensions of the physical structure are small compared with the "characteristic length" of the electromagnetic field. In this case the time derivative term in the wave equation can be neglected, leaving only the ∇^2 term. This is called the "quasistatic" approximation because the field satisfies the Laplace (static field) equation, even though all components are time varying. The quasistatic approximation is applied, for example, in calculating the values of alternating current circuit elements such as coils and capacitors. Eddy current testing is typically performed at frequencies lower than 10 MHz, with probe coil and defect dimensions less than 1 cm. In the air medium outside the metal testpiece, the characteristic length is the wavelength λ. At usual eddy current test frequencies, λ is in the range of kilometers, so the quasistatic approximation is always applicable in the air medium. However, in a highly conducting testpiece, the time derivative terms in the wave equation reduce to

$$\omega^2\mu\left(\varepsilon + \frac{\sigma}{i\omega}\right) \cong -i\omega\mu\sigma \qquad (17)$$

in the frequency range for eddy current testing[11] and convert the wave equation into the diffusion equation, where the characteristic length is the skin depth[2,3]

$$\delta = \sqrt{\frac{2}{\omega\mu\sigma}} \qquad (18)$$

At 1 *MHz* in aluminum δ = 0.5 *mm*, and it is much smaller in magnetic metals, so that the quasistatic (Laplace) approximation is not applicable in the metal at the higher range of test frequencies. In this range, penetration of the a-field into the testpiece is governed by the skin depth. At frequencies in the very low kilohertz range the quasistatic approximation does apply for typical probe coil dimensions, and the a-field penetration is then governed by the coil dimensions rather than by the skin depth.[42]

Certain types of two-port probes, such as the reflection probe in Fig. 2c, are also axisymmetric and the vector potential fields of the two coils again have only an azimuthal component. Since the a-field in Fig. 3b has coil 1 excited and coil 2 open circuited, and since the open-circuited coil does not perturb the drive coil at eddy current frequencies, the Dodd and Deeds analysis can be applied directly to coil 1. A particularly simple form of axisymmetric two-port probe is frequently used in some eddy current sensors for material processing control.[24–26] Here the drive coil is a long solenoid encircling a cylinder of the material under test and the pickup coil is a short single-turn solenoid at the midpoint of the drive solenoid, where the a-field is uniform and is described by a simple closed form expression.

A more complicated example is the differential reflection probe of Fig. 4a. Here there is a pair of circular counterwound pickup coils, placed side by side and connected in series. In Fig. 2c the larger (drive) coil is labeled 1 and the smaller (pickup) coil is labeled 2. From Fig. 3 this means that the a-field is calculated by exciting the large coil *in the absence of the defect*, and the b-field by exciting the small coil *in the presence of the defect*. Since coupling between two coils is always reciprocal, the transfer impedance can also be calculated with the large coil labeled 2 and the small coil 1. The a-field is then obtained by exciting the small coil in the absence of the defect, and the b-field by exciting the large coil in the presence of the defect. Because both coils are axisymmetric this change of coil labeling does not reduce the difficulty of solving the b-field problem. In the case of the differential reflection probe (Fig. 4a), there is, however, an advantage in labeling the differential pickup coil 1 and the drive coil 2. In doing this, the simpler a-field problem is excited by the more complicated coil geometry 1, while the more difficult b-field problem is excited by a simple axisymmetric coil. Since the two axisymmetric coils in 1 are driven in series by the same current I, their contributions to the

a-field can be calculated separately by the Dodd and Deeds formulation, then superimposed.

Evaluations of the a-field by analytical methods have been reported for some complicated air core structures: coil axis horizontal,[9,10] rectangular-shaped coil with rounded corners and horizontal axis,[13] and nonrectangular winding cross section.[14] Some of these methods, as in Ref. 28, can be applied to D-shaped coils oriented either horizontally or vertically.

For more complicated air core coil structures (coils located close to an edge of the testpiece, etc.) the a-field can generally be obtained only by using numerical methods (finite difference, finite element, volume element, boundary-element hybrid, etc.).[43–45] Finite difference was the only method available during the early development of electronic computers but is now rarely used for problems in eddy current NDE. But Section 3.4 does show how this method can be usefully applied in connection with certain analytic approximations. Finite element and boundary element, sometimes combined in a hybrid formulation, are now the most widely used methods for solving the a-field problem. Extensive reference listings are given in Refs. 43–45, with a detailed comparison of finite element and boundary element given in Ref. 45. Generally speaking, the boundary-element procedure reduces the amount of discretization required for problems involving only isotropic and homogeneous materials, compared with finite element. This advantage, which derives from the use of free-space Green's functions in the various geometrical regions of a test geometry, leads to a frequent preference for the boundary-element method, especially for testpieces of complex shape[46] and probe location close to an edge.[47,48] In such cases, boundary element is often combined with another numerical procedure: hybrid volume-boundary element[49] and hybrid finite-boundary element.[50]

2.2.2. Ferrite Core Coils

Ferrite core probes[11,12,15,30–32] are now widely used to concentrate or otherwise modify the spatial distribution of the a-field. Figure 4b illustrates a probe of this type that is specially designed to produce a spatially uniform a-field in the vicinity of a defect.[15,16] (It is shown in Section 3.3 that this probe can greatly simplify the analytic evaluation of ΔZ.) For ferrite core probes, use of one of the numerical methods listed above is imperative. Boundary element and finite element are still the preferred methods, but volume element has also been used.[11,12]

The remote field eddy current technique for locating defects in ferromagnetic tubes has been modeled by the finite-element method[21–23] and by a boundary-element
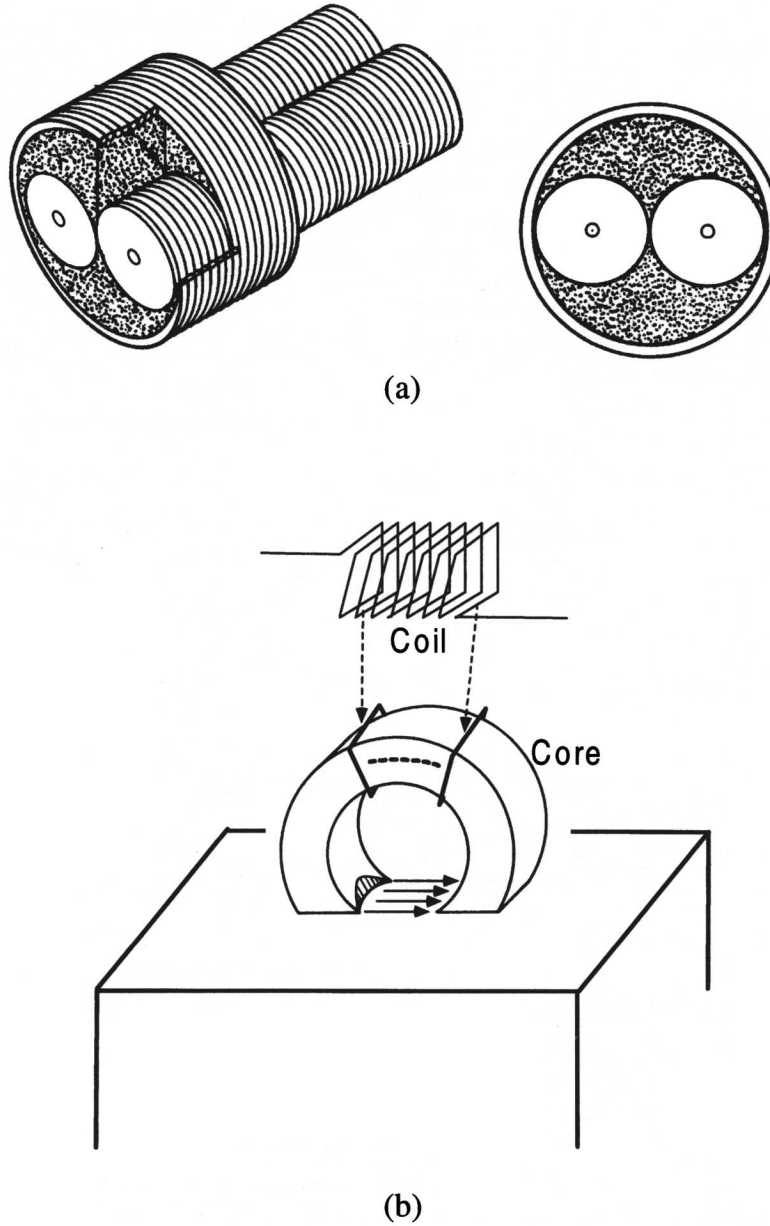
(a)

(b)

Fig. 4. More complex probe geometries. (a) Differential reflection probe. (b) Uniform-field ferrite probe.

mesh, using an iterated Born approximation.[51] In modeling this application, some difficulties arise from uncertainty as to the value of the permeability and the extent of its spatial variations.[22] When the permeability is inhomogeneous, only the finite-element method is applicable. Although ΔZ relations have not yet been applied to this type of probe, [16] is usable in principle once the fields excited by the drive and pickup coils have been evaluated numerically.

2.2.3. Photoinductive Probe Characterization

In (10a) and (10b) and (16a) and (16b) the a-field (the interrogating field) characterizes the properties of the probe itself. An accurate evaluation of this field is a prerequisite to an accurate evaluation of the b-field, which characterizes the probe–defect interaction. To model the defect signal ΔZ correctly, both the a-field and the b-field must be known precisely. It has been observed exper-

imentally, however, that having a precise mathematical field model is not sufficient to guarantee accurate modeling of ΔZ. Nominally identical probes have been found to give signals that differ by as much as 35%, even though the probe inductances were identical to better than 2%. For truly quantitative NDE it is therefore essential to measure the a-field distribution experimentally. This can be done, for example, by the photoinductive method, where the probe under test is placed over a "witness plate" consisting of a carbon layer deposited on a nonmetallic substrate. A laser beam focused on the carbon layer from below induces a localized temperature and conductivity change.[52,53] Substituting

$$\delta\varepsilon = \frac{\delta\sigma}{i\omega} \qquad (19)$$

from (11) and the Burrows' approximation for a small inclusion [from (24) in Section 2.3.1] into (10b) shows that localized heating by the laser beam generates a ΔZ that is proportional to E_a^2 at the position of the laser spot. Scanning the laser beam over the witness plate generates a mapping of the electric part of the a-field in the carbon layer.

Reference 53 shows explicitly how the three-dimensional electric a-field in the absence of the carbon layer can be determined from photoinductive mapping of the electric field in the layer. Since this electric field $\vec{E}$ is equal to the vector potential $\vec{A}$ inside the test piece, the corresponding three-dimensional magnetic a-field (used in the modeling techniques described here) can be calculated from $\vec{A}$.[39-41]

For simple probe geometries the measured and calculated field distributions have been shown to be in good agreement. The technique has proved to be useful for directly characterizing probes in field operations and for quality control in probe manufacture.

2.3. Probe–Defect Interaction Modeling

2.3.1. General Considerations

In Section 2.2 a review was given of analytic and numerical methods for obtaining the a-field distribution. The b-field distribution is much more difficult because of the more complicated shape of the flawed testpiece.

Exact and numerical solutions are available in some cases, such as dimensional defects (such as errors in the dimensions of a plate, a cylinder, etc.) and homogeneous material property defects in cylinders.[26,54] Dodd and Deeds[39-41] provide a general catalog of exact analytic a- and b-field solutions for such problems in layered plates and cylinders.

For the particularly simple case in Ref. 26, a two-port probe consisting of a long solenoidal drive coil and a single-turn pickup coil, both closely fitted a long cylindrical testpiece, is used to sense property changes during processing. The change in transfer impedance can be found by simply calculating the change in flux linkage through the pickup coil, so that the change ΔZ_{21} is expressed completely, without using (16), in the form[25]

$$\Delta Z_{21} = -\frac{1}{I^2} \int_{\text{pickup coil}} \vec{E}^{(s)} \cdot \vec{j}\, dV \qquad (20)$$

where I^2 is the current in the winding of the drive coil, $\vec{j}$ is the current density in the pickup coil, and

$$\vec{E}^{(s)} \equiv \vec{E}_b - \vec{E}_a \qquad (21)$$

is the change in electric field (the "scattered" field) due to the change in material properties. The integral is performed over the entire winding of the pickup coil. To evaluate (20) for some more complex geometries, the exact analytic solutions of Dodd and Deeds[39-41] may also be used in (20).

Although few analytical b-field solutions exist, an increasing number of numerical solutions is becoming available in the literature. Some examples are finite element[18,55-57] volume element,[58-61] and boundary element[62,63] (collocation).[64-69] Formulation (20) may also be used with these numerical solutions. But for numerical rather than analytical solutions, there is an advantage in using ΔZ. In effect, using the ΔZ relations reduces the precision required in computing both the a- and the b-field. This can be demonstrated by assuming a small mean percentage error ρ in the computed fields $\vec{E}_a$, $\vec{H}_a$ and $\vec{E}_b$, $\vec{H}_b$. For one-port probes it can be seen from Ref. 4 that Z_a and Z_b then have a percentage error 2ρ; and, from (10), ΔZ has the same percentage error. In contrast, if ΔZ is evaluated from the one-port version of (20), the percentage error in ΔZ is

$$\rho' = \frac{Z_b - Z_a}{\Delta Z}\rho \qquad (22)$$

This is much larger than ρ when the defect is small

$$\Delta Z << Z_a, Z_b \qquad (23)$$

Stated in words, evaluation of the probe impedance change from (20) requires taking a small difference between two large quantities. Evaluation from the ΔZ relation does not have the limitation. This argument may also be applied to two-port probes.

Since the integrals in the ΔZ relations are localized to the region of the defect, a second advantage of this format is that the computational load is reduced by

restricting discretization to the locality of the defect.[61,69] This feature can be exploited in all of the volume-element,[58–61] boundary-element,[62–69] and finite-boundary element[50] computational procedures. For geometrically simple testpiece shapes, where an analytical form of the Green's function for the bounded body is available, only the region of the defect need be discretized when using the boundary element method.[10,61,69] But in the general case, it is necessary to use the unbounded Green's function and discretize both the region of the flaw and the boundary of the testpiece.

Other advantages arising from the "localization" property of the ΔZ relations are that it facilitates intuitive physical reasoning and, by extension, development of analytical approximations. Four types of approximation are most commonly used.

2.3.1.1. Quasistatic Approximation. If the volume of an inclusion or a void is sufficiently small that the a-field is essentially constant in the neighborhood of the defect, the quasistatic approximation is valid and the b-field has a static field distribution in and around the defect. For an inclusion or a void of ellipsoidal shape, the solution is particularly simple.[70,71] The b-field is then uniform within the defect volume V_F in (10b), (16b) and the integration reduces to multiplication by V_F, giving Burrows' result.[1] For a spherical inclusion, with properties μ_b, ε_b, in a testpiece with properties μ_a, ε_a the b-field within the defect is related to the a-field at the position of the defect by

$$H_b = \frac{3\mu_a}{\mu_b + \mu_a} H_a, \qquad E_b = \frac{3\sigma_a}{\sigma_b + \sigma_a} E_a \qquad (24)$$

where approximation (11) has been used. Substitution into (10b), (16b) gives Burrows' formula. A complete tabulation of the multiplying factors to be used in (24) for ellipsoidal defects is given in Ref. 71. Other relevant information is available in Ref. 1. A more general approach (low-frequency asymptotics) extends the quasistatic approximation to defects of arbitrary shape.[72]

2.3.1.2 Born Approximation. If an inclusion has properties μ_b, σ_b that differ only slightly from the testpiece properties, the Born approximation may be used in evaluating (10b), (16b). For

$$\delta\mu \equiv \mu_b - \mu_a << \mu_b, \mu_a$$
$$\delta\sigma \equiv \sigma_b - \sigma_a << \sigma_b, \sigma_a \qquad (25a)$$

the relation between the b- and the a-fields is

$$\vec{E}_b = \vec{E}_a + \delta\vec{E}, \qquad \delta\vec{E} << \vec{E}_b, \vec{E}_a$$
$$\vec{H}_b = \vec{H}_a + \delta\vec{H}, \qquad \delta\vec{H} << \vec{H}_b, \vec{H}_a \qquad (25b)$$

where $\delta\vec{E}$, $\delta\vec{H}$ are of the same order as $\delta\mu$, $\delta\sigma$. Substitution of (25a), (25b) into (10a), (10b) shows that, to first order in the δ quantities, ΔZ can be obtained using the approximation

$$\vec{E}_b, \vec{H}_b \cong \vec{E}_a, \vec{H}_a \qquad (26)$$

This result is evident from (24) for the case of a small, weak spherical inclusion. The advantage of the Born approximation over the quasistatic approximation is that it is applicable to weak inclusions of arbitrary shape and size. But the Born method cannot be used with surface integral formulations of the ΔZ relations. Substitution of (26) into (10a), (16a) makes this clear. In the surface integral format, the ΔZ calculation is most easily approximated when the testpiece skin depth is much smaller than the dimensions of the testpiece and the defect.

2.3.1.3. Variational Approximation. This third member in the trio of most widely used approximations in physics and engineering has also been applied to the evaluation of ΔZ,[73–75] although not yet fully developed. Here, both the volume and the surface forms, (10a) and (10b), (16a) and (16b), of ΔZ have been reformulated as variational expressions. Substitution into these expressions of approximate solutions to the a- and b-fields, with a small mean percentage error ρ, yields a ΔZ with an error of order ρ^2. This property facilitates the use of physically intuitive field approximations and also has important implications for numerical evaluations of ΔZ.

2.3.1.4. Thin Skin Approximation. This approximation, inspired by the methods of microwave circuit theory,[2,3] applies when the skin depth (18) of the testpiece is much smaller than the dimensions of the defect. It is therefore restricted to surface-breaking, or very nearly surface-breaking, defects of various kinds—cracks, EDM notches, pits, voids, etc. Figure 5 illustrates, for the case of a surface-breaking crack or EDM notch, the three steps involved in analyzing this type of problem. Figures 5a and b define, respectively, the a-field and b-field problems for the real physical configuration. The b-field problem is approximated through the intermediate step defined by Fig. 5c, for the idealized physical configuration of a perfectly conducting flawed testpiece. The tangential magnetic field excited by the probe at the defect/testpiece surface is first calculated for this idealized problem. The actual tangential electric field at this surface is then obtained, in the thin skin approximation, from the skin impedance[2,3] for the lossy testpiece material,

$$Z_s = \frac{1+i}{\sigma\delta} \qquad (27)$$
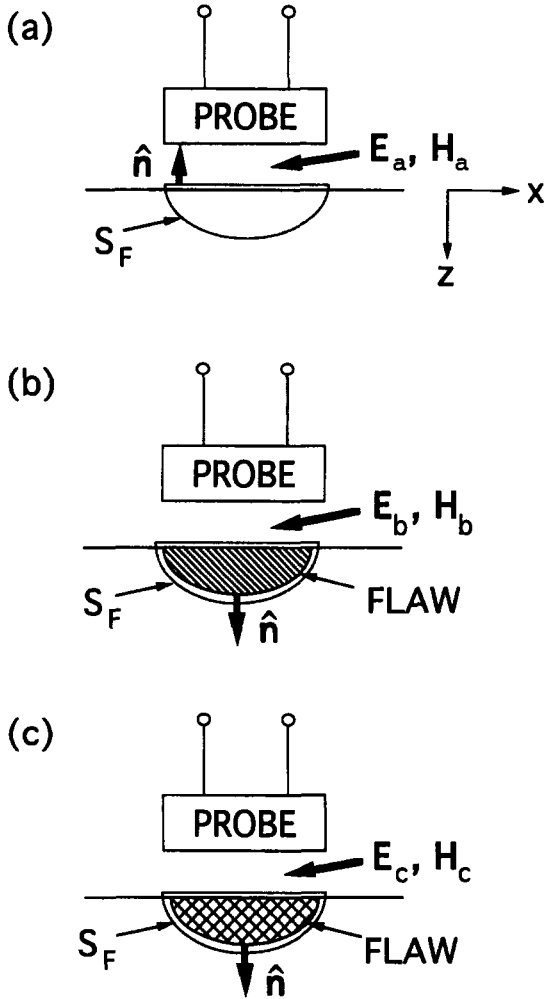
applied to all points on the interior walls of the defect

(a)

PROBE

$\hat{n}$ ↑ ⟵ E_a, H_a

S_F

⟶ X

Z

(b)

PROBE

⟵ E_b, H_b

S_F FLAW

↓ $\hat{n}$

(c)

PROBE

⟵ E_c, H_c

S_F FLAW

↓ $\hat{n}$

Fig. 5. Probe–defect configurations for the ΔZ analysis. (a) Unflawed testpiece. (b) Actual flaw. (c) Idealized flaw.

and the upper surface of the testpiece in Fig. 5b. [Corrections for the tip and the upper edges (or lips) at the mouth of a surface breaking crack or EDM notch[63,76] are discussed in Section 3, which gives full details of the above procedure.]

It is useful at this point to examine briefly the nature of air/metal boundary conditions in eddy current problems. The thin skin approximation begins with a calculation of the probe field in the presence of a lossless flawed testpiece. In microwave circuit theory, the solution to such an idealized problem is a Maxwell, or nonquasistatic field; in eddy current theory the solution is quasistatic. Section 2.2.1 defined the quasistatic approximation with reference to the wave equation in air and the diffusion equation in metal. It was seen that this approximation is always valid in the air medium but not, for the higher test frequencies, in the metal medium.

In the idealized defect problem (Fig. 5c) the magnetic field is quasistatic in the air and zero in the metal. To understand more clearly the physical nature of the probe field in this idealized case, it is useful to consider the lossless Maxwell curl relations at a test frequency ω,

$$\vec{\nabla} \times \vec{E} = -i\omega\mu\vec{H}$$
$$\vec{\nabla} \times \vec{H} = i\omega\varepsilon\vec{E} \tag{28}$$

and to substitute the power series expansions [77]

$$\vec{E} = \sum_n \omega^n \vec{E}^{(n)}$$
$$\vec{H} = \sum_n \omega^n \vec{H}^{(n)} \tag{29}$$

The quasistatic fields, as defined previously are clearly the zero-order terms $\vec{E}^{(0)}$ and $\vec{H}^{(0)}$ in (29), so that the quasielectrostatic and quasimagnetostatic fields are uncoupled in (28). In this order, the probe behaves as a lumped circuit element—a lossless inductor near a lossless metal screen. The quasimagnetostatic part of the field is generated by current flow in the coil; the lowest-order contribution to the electric field of the probe arises from the voltage drop across the inductive reactance of the coil. Although the resulting lowest-order E field has, in effect, a quasistatic spatial distribution, it is proportional to ω [first order in (29)] because it is excited from the current by way of the inductive reactance ωL of the coil.

For the actual problem [Fig. 5(b)] both the coil winding and the testpiece have finite conductivity, with

$$i\omega\varepsilon \rightarrow i\omega\varepsilon + \sigma$$

in (28), so that the quasistatic fields $\vec{E}^{(0)}$ and $\vec{H}^{(0)}$ are coupled. In eddy current modeling, the contribution of the winding conductivity is normally ignored. Following Dodd and Deeds[41–43] and the various numerical field calculations, the coil current is taken as an ideal current filament. The testpiece conductivity, on the other hand, is included. In the thin skin approximation this inclusion of testpiece losses is simplified by using the skin impedance (27), as outlined above.

An alternative approach to the thin skin approximation was developed in connection with the alternating current potential difference (ACPD) method for the detection of surface-breaking defects. In its first realization this method interrogated the surface defect with a uniform current injected into the testpiece by a pair of remote electrode contacts. The defect was detected by means of a pair of point voltage contacts, aligned parallel to the direction of the unperturbed interrogating current. Perturbation of the measured voltage difference indicated the presence of a defect. Probe interaction with a surface

breaking crack was modeled in the thin skin approximation by means of the "unfolding" technique.[78] This approach was based on the analytical proof that, in this measurement, the distribution of the eddy current field over the surface of the testpiece is described by the two-dimensional vector Laplace equation. The same description also applies to the current distribution on the inner surfaces of the surface crack. This three-dimensional thin skin geometry was then unfolded into two dimensions by bisecting the flawed testpiece along the plane of the crack and then flattening each part of the bisected crack into a two-dimensional problem plane. Using the required continuity conditions at the tips and edges of the half-crack sections, it was shown that the "unfolded" vector Laplace solution in two dimensions corresponds to a known hydrodynamic flow problem.

In essence, use of the unfolding technique requires interrogation of the defect by an essentially uniform eddy current field. This condition was met in the earliest experiments by placing the current injection electrodes far from the defect. Because of difficulties in certain environments with contacting the voltage difference pickup probe, it was replaced by a horizontal pickup coil to sense the horizontal component of the fringing magnetic field above the crack.[27,28] Eventually, for the same practical reason, the drive current contacts were also replaced by a drive coil designed to provide a uniform eddy current field distribution.[13] This approach, called the alternating current field measurement (ACFM) approach, then corresponds to use of a two-port eddy current probe, as described in Section 2.1.2. It might use a driver of the form shown in Fig. 4b. Another probe of similar form evolved from a Hall probe detection scheme for observing the fringing magnetic field of a surface crack interrogated by the eddy current field of a large drive coil.[29,30,79] This type of probe has a vertical drive coil and a horizontal pickup coil. In Refs. 13, 27, and 28, both the drive and the pickup coils are horizontal. The "unfolding" approach to modeling the probe–defect interaction requires that the eddy current field near the defect be in a region far removed from the source fields, as in Ref. 78. When the current injection electrodes are replaced by a drive coil this condition is no longer strictly observed. A detailed analysis of the air–metal interface and the fringing field of a crack, in Ref. 27, addresses this question.

Use of the quasistatic approximation (with the magnetic field in air represented as the gradient of a scalar potential) for the surface-breaking crack problem is detailed in Section 3.1.[20,80] To treat the complex testpiece shapes now encountered during in-service eddy current inspection and computer simulation,[81] an extended scalar potential method had been developed.[82] This approach is shown to be very convenient for treating ferrite core probes and very effective in modeling edge effects.[83] It permits the use of the boundary-element method for these types of problems, with a reduced computational load but without sacrificing flexibility.

The following subsections give brief overviews of analytic approximations and exact numerical evaluations for the general classes of defects listed in Section 1, as well as for liftoff and tilt. For each topic a sampling of references is listed in chronological order. The ΔZ relations of the present paper are applicable to all of these examples cited but have not always been used explicitly in the cited references.

2.3.2. Surface Cracks and Slots

Because of their potential importance, natural surface cracks, and notches or slots (fabricated by electrical discharge machining, EDM, as experimental simulations of cracks), have always been the subject of intensive modeling studies. Both rectangular and semielliptical (or semicircular) notches have been examined. Approximate analytical methods have been developed for both the thin skin (skin depth $\delta \ll$ crack depth a) and the thick skin (skin depth $\delta \gg$ crack depth a) regimes. In addition, numerical methods have now been developed for arbitrary ratios of skin depth to crack depth.

When the diameter of an eddy current probe is small compared with the skin depth of the testpiece material, it is the probe diameter that determines the penetration of the a-field into the material.[38,42] In such instances, the ratio of the probe diameter to the crack depth can strongly influence the choice of analytic approximation. Two important cases arise in the thin skin regime: probe diameter $\gg$ crack depth (uniform field interrogation) and probe diameter $\ll$ crack depth (localized field interrogation). It is shown in Section 3 that uniform field interrogation accurately senses the depth of a crack but does not clearly display the length of a crack. In contrast, localized field interrogation accurately senses the length (or surface image) of a crack but does not clearly display its depth. This behavior, which can be explained by noting that a crack (or EDM slot) is in effect a very small short circuited cutoff waveguide. In localized field interrogation the probe preferentially excites very strongly cutoff modes that do not reach the bottom of the crack. This behavior, illustrated explicitly in Reference 80 for a rectangularly shaped EDM slot, will be seen to play an important role in the inversion procedure.

2.3.2.1. Approximate Analytical Methods. 2.3.2.1.1. Thin Skin Regime. Reference 84 distinguished between thin skin (large a/δ) and thick skin (small a/δ) modeling

approximations. Here a is the crack depth and δ the skin depth. Both two-dimensional cracks (infinite surface length) and three-dimensional cracks (finite surface length) were modeled. The a-field (interrogating field) was assumed in all cases to be uniform over the surface of the testpiece. For a two-dimensional crack the ΔZ integral over S_F reduced to a line integral around the contour enclosing the crack cross section. Using the thin skin surface impedance on the crack walls, performance of this integral separated the contributions of the crack-wall losses and the crack opening. Contributions of the crack lips and the crack tip[63,76] were added as correction terms. For a three-dimensional crack the b-field was obtained from the unfolding model[78] for part-circular surface cracks. This model describes the surface field by a potential that is continuous at the fold line. This assumption has been verified for ferromagnetic metals but not for nonferrous metals.

In Ref. 85, previous results were reviewed and the modeling was extended to a rectangularly shaped surface-breaking defect (EDM slot) interrogated by an a-field that was spatially nonuniform on the testpiece surface. This analysis applied the Born approximation to the tangential magnetic field in the mouth of the crack. That is, H_T in the crack mouth was assumed to be the same as the field that would have existed in the area coinciding with the crack mouth, but on the surface of an unflawed testpiece.

In the second approximation, the magnetic field in the interior of the flaw was calculated for the case of a perfectly conducting testpiece. Losses in the flaw walls were then introduced by means of the skin impedance of the actual testpiece material (27). This model was used to obtain the response (flaw profile) of an absolute probe scanned along the length of a rectangular EDM slot.[86] The method was extended in Ref. 87 by applying the formal thin skin perturbation theory of Ref. 9 and including the possibility of probe scans that are not centered on the plane of the EDM slot. A detailed study of the effects of EDM slot closure[60] was based on the use of the thin skin theory of Ref. 27 to obtain the b-field without restriction to the Born approximation used in Ref. 85. In Ref. 88, Hartfield and Bowler present a more accurate version of the two-dimensional crack model in Ref. 84, calculating the b-field by the Wiener–Hopf technique. Further applications of this technique are discussed in Section 2.3.3.

2.3.2.1.2. Thick Skin Regime. The seminal work of Burrows[1] falls into this category. In this case, surface-breaking cracks and EDM notches were modeled approximately by bisecting a thin ellipsoidal void and placing it at the testpiece surface. In Ref. 84 two-dimensional and three-dimensional cracks were modeled by using the hydrodynamic flow analogy. This analogy and Burrows' ellipsoidal void model were briefly reviewed in Ref. 85. A variational approach[89] extended the treatment of ellipsoidal voids in Ref. 1 to voids of arbitrary shape. In principle, this technique could be applied to surface breaking cracks of arbitrary shape. The unfolding technique,[78] as applied to the ACFM method,[13,27,28] was applied to model the b-field of a surface breaking crack in the thin skin regime. For the thick skin regime, Ref. 90 used the hydrodynamic flow analogy to model the ACFM response of a semielliptical surface breaking crack. Beissner et al.[29] applied the same method to obtain the b-field for a semicircular surface breaking crack.

2.3.2.2. Numerical Methods. In recent years there has occurred a remarkable evolution and expansion of the applications of numerical methods to eddy current NDE.[81–83,91–97] These techniques are especially useful when the testpiece has a complicated shape. But numerical methods are also advantageous even when the testpiece shape is simple, because these methods are applicable even in the intermediate skin regime. However, despite this flexibility of numerical methods, the computational efficiency can always be improved by using the thin skin approximation when appropriate. Use of a scalar potential model also improves the computational efficiency. The finite-difference method was first applied in evaluating the scalar potential model of Ref. 85, for semicircular and semielliptical surface breaking cracks. Subsequently, an improved scalar potential model[64,87] was developed for boundary-element modeling of three-dimensional cracks (asymmetric probe scans) in a flat testpiece. And, more recently, an extended scalar potential theory,[82] by placing the model on a completely rigorous basis, permitted smooth performance of boundary-element calculations of the b-field, even in the presence of such geometric singularities as edges and corners.

2.3.2.2.1. Finite Difference. Although this numerical method is now rarely used in eddy current modeling, the scalar potential approach of Ref. 85 is sufficiently simple to merit application of a very simple numerical method for solving the Laplace scalar potential problem in the interior of a crack or an EDM slot. Reference 80 presented flaw profile curves for a rectangular EDM slot, calculated from the analytical model of Ref. 85. This was compared in Ref. 91 with profile curves obtained for the same problem using the finite difference method. Curves for semielliptical EDM slots, obtained by finite differences, were also presented in the same paper. These results were all for an absolute probe. Similar results were given in Ref. 20 for a two-port (reflection) probe, with the numerical procedure extended to the three-dimensional case

(asymmetric probe scans), as in Refs. 64 and 87. This work is detailed in Section 3 as an illustration of the forward problem.

2.3.2.2.2. Finite Element. Finite-element models[92-94] have recently been developed for surface-breaking cracks and EDM notches. A reciprocity relation was used to show that (20) is equivalent to the electrical terms in (10b), where the integral is performed only over the flaw region, with the advantages noted in Section 2.3.1. These new models can also extend the treatment to two-port probes and evaluate ΔZ from the electrical term in (16b).

2.3.2.2.3. Volume Element. Conversion of (20) to an integral over only the flaw region has also been applied to volume element modeling.[59,61,95] Because VEM is based on the use of a Green's function, this reduces the amount of discretization required.

2.3.2.2.4. Boundary Element. This approach is much more widely used at present than volume element for modeling eddy current problems. References 64 and 87 applied BEM to the model in Ref. 85, with an improved scalar potential formulation and application to more complex geometries. A general review of the boundary-element method was given in Ref. 96. References 65, 66, and 67 illustrated application of the method to a complex geometry of great practical importance—the corner crack. An ideal, or zero-thickness, surface-breaking crack was studied in Ref. 69. By considering the electromagnetic continuity conditions across the plane of the crack, it was shown that the jump in the transverse electric field at the crack is given by the surface gradient of a surface scalar function p, now commonly known as the Bowler potential,

$$\vec{E}_t^+ - \vec{E}_t^- = -\frac{1}{\sigma} \nabla_s p \qquad (30)$$

where σ is the testpiece conductivity. The crack is represented by an equivalent secondary source consisting of a layer of current dipoles directed normal to the crack surface,

$$\vec{p} = \hat{n}p \qquad (31)$$

The function p is obtained by solving the scattered field problem by BEM, with the current boundary condition

$$J_n = 0 \qquad (32)$$

at the crack, and constructing the b-field as the sum of the a-field and the scattered field. The electrical term in (10b) then becomes

$$\Delta Z = -\frac{1}{I^2} \int_{S_o} \vec{E}_a \cdot \vec{p}_b dS \qquad (33)$$

where S_o is the surface of the crack and a subscript b has

been appended to the dipole layer distribution function as an indication that this is associated with the b-field. Reference 97 reviews the application the extended scalar potential representation[82] to a complex surface breaking crack problem. The status of software implementation for in-service eddy current inspection and simulation, based on the extended scalar potential method, is reported in Ref. 81.

2.3.3. Subsurface Cracks

2.3.3.1. Approximate Analytical Methods. In the class of subsurface cracks the thin skin regime is not relevant, except as a description of an almost surface-breaking crack. The following examples therefore consider the skin depth to be comparable to or greater than the crack dimensions. Burrows' ellipsoidal void model[1] applies to deep subsurface cracks in the thick skin regime. There exist only a few references that deal analytically with more realistic subsurface crack problems. Three of these applied the Wiener–Hopf technique to solving b-field problems for subsurface cracks. Undercladding cracks were treated in Ref. 98 and pages 68–81 in Ref. 99, and subsurface cracks in noncladded testpieces were studied in Ref. 100.

2.3.3.2. Numerical Methods. 2.3.3.2.1. Finite Element. References 55 and 99, Appendix F, apply this method to subsurface cracks, the first citation for subsurface in uncladded testpieces and the second for interface cracks in cladded testpieces. General three-dimensional FEM software suitable for subsurface cracks and other general problems is described in Ref. 101.

2.3.3.2.2. Volume Element. The surface crack model in Ref. 61 could be extended to subsurface cracks, and Ref. 102 applied the volume-element method to a general subsurface defect. This could be specialized to subsurface and interface cracks.

2.3.3.2.3. Boundary Element. The surface crack model in Ref. 69 could be extended to subsurface cracks, and the general boundary-element procedure described in Ref. 96 could be specialized to subsurface and interface cracks.

2.3.4. Other Types of Defects—Pits, Voids, Inclusions, and Nonlocal Inhomogeneities

2.3.4.1. Approximate Analytical Methods. In the thick skin regime, the ellipsoidal model of Ref. 1 is applicable to pits, voids and inclusions, and Ref. 89 could be applied to arbitrarily shaped defects of the classes listed under this heading, again in the thick skin regime. Some of the other analytical references cited here are for the
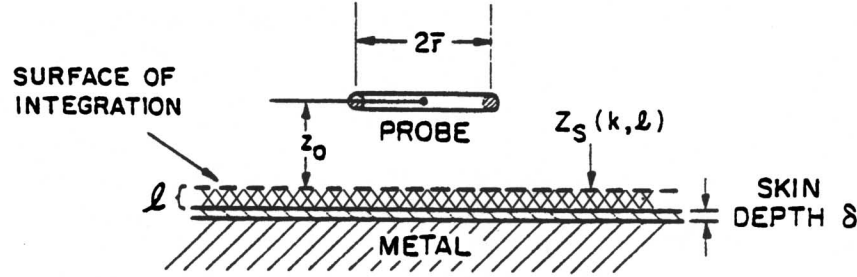
Fig. 6. Single surface layer of thickness l (after Ref. 99).

thin skin regime: corrosion and other inhomogeneities were studied, in Ref. 103 using spatial frequency analysis, pits in the form of a spherical cap cavity interrogated by a uniform current field in Ref. 104, spatial frequency (angular spectrum) analysis at low temporal frequencies of spheroidal defects,[30] shallow flat-bottomed holes interrogated by a uniform field probe,[16] low-frequency asymptotic solutions for irregularly shaped inhomogeneities,[72] corrosion pits interrogated by the remote field eddy current method and modeled in the Born approximation,[51] and hemispherical pits interrogated by an ACFM probe.[105]

2.3.4.2. Numerical Methods. The finite-element method was applied to a through hole in a tube wall[18] and to oxide buildup in nuclear steam generator tubing.[106] Sophisticated numerical software is now available[62,82,94–96] for a much wider range of modeling applications to all classes of defects in this category.

2.3.5. Layers and Topography

2.3.5.1. Analytical Methods. 2.3.5.1.1. Layers. The surface (and subsurface) layer b-field problem is of very significant importance for quality control of deposited layers, and for detection and characterization of defects in the form of a layer or layers—i.e., corrosion. This is one of the few b-field problems for which there exists a rather complete set of exact analytical solutions. The earliest examples[39–41] deal with both planar and cylindrical geometries. Equation (20) gives ΔZ in terms of an integral over the probe coil. But this is equivalent to taking the difference of Z_b and Z_a. For small ΔZ it is advantageous precisionwise [see (22) and (23)] to evaluate the a- and b-fields in the layer and then apply the ΔZ relation (10a) and (10b).

In the references cited, the field solutions are obtained in the form of Fourier–Bessel expansions, which limit the method to axisymmetric problems. A more general procedure is the spatial frequency (or angular spectrum) method,[30,99,103] where the fields are expressed as

an angular spectrum of plane waves. In this case, the E and H fields are expanded directly rather than using vector and scalar potentials

$$\vec{E}(x, y) = \frac{1}{2\pi} \int_{-\infty}^{+\infty} \int_{-\infty}^{+\infty} \vec{e}(k_x, k_y)e^{i(\vec{r}\cdot\vec{k})} \, dk_x \, dk_y \tag{34a}$$

$$\vec{H}(x, y) = \frac{1}{2\pi} \int_{-\infty}^{+\infty} \int_{-\infty}^{+\infty} \vec{h}(k_x, k_y)e^{i(\vec{r}\cdot\vec{k})} \, dk_x \, dk_y \tag{34b}$$

where z is the layering direction (Fig. 6) and the Fourier components individually satisfy Maxwell's equations. In this way, the quasistatic approximation is automatically introduced as the angles of incidence of the angular plane waves increase. In the general case, Fourier components polarized both perpendicular and parallel to the plane of incidence are required. Axisymmetric probe coils require only parallel polarized components. For a one-port probe the a- and b-fields in (10a) are both expanded as in (34), and S_F lies along the dashed line in the figure, with closure at infinity where the quasistatic field makes no contribution (Appendix A). Only the surface-tangential field components enter into the integrand of (10a) and the E-field components can be related to the H-field components through the a-subscripted and b-subscripted surface impedances at the dashed line in the figure, where the cross-hatched region is a deposited layer and the region labeled "Metal" is the uncoated testpiece. The final result is

$$\Delta Z = -\frac{1}{I^2} \int_{-\infty}^{+\infty} \int_{-\infty}^{+\infty} \delta Z_s(\vec{k})\vec{h}_{ta}(\vec{k}) \cdot \vec{h}_{tb}(-\vec{k}) dk_x \, dk_y \tag{35}$$

with

$$\delta Z_s = Z_{sb} - Z_{sa}$$

where the b-configuration is as shown in Fig. 6 and $l = 0$ for the a-configuration. The subscript t denotes magnetic

fields in the xy plane. This formalism is applicable to nonaxisymmetric probes, both one- and two-port probes, and multiple layers. Layers with continuously variable properties are treated in Refs. 107 and 54.

Modeling of corrosion layers in lap junctions deserves special mention at this point. Defects of this type are commonly modeled as subsurface air gap layers because of the low conductivity of corrosion products.[108]

2.3.5.1.2. *Topography*. Eddy current probes have been designed to determine the position and orientation of surface topographical features such as steps and edges.[109] Figure 7 illustrates a crossed differential two-port probe used for this purpose. The two differential pickup pairs are read individually. When the probe is oriented such that one pair is parallel and the other perpendicular to an edge, the first pair does not respond to the edge and the second pair has a maximum output. But small changes in the orientation of the edge are easily detected by the first pair.[110,111] Figure 8 illustrates the response of this probe to a curved step.

In a topographical problem the angular Fourier components are coupled by the topographical relief and (35) is not applicable. But, in the spirit of the thin skin approximation,[84–88] field nonuniformities near steps and edges are ignored to a first approximation, and in the piecewise uniform regions of the topographical structure the surface impedance is defined as for a normally incident plane wave—a reasonable assumption when the fields have slow spatial variations. Substituting this spatially varying surface impedance into (16a) then yields

$$\Delta Z(x_o, y_o) = \frac{1}{I^2} \int\int Z_s(x, y)\vec{H}_{1a}(x, y) \cdot \vec{H}_{2b}dxdy \qquad (36)$$

This approach yields satisfactory qualitative agreement with experiment.

2.3.5.2. *Numerical Methods*. A wide range of sophisticated software is now available for modeling layer and topographical problems. The extended scalar approach to the boundary element method[82] is especially worthy
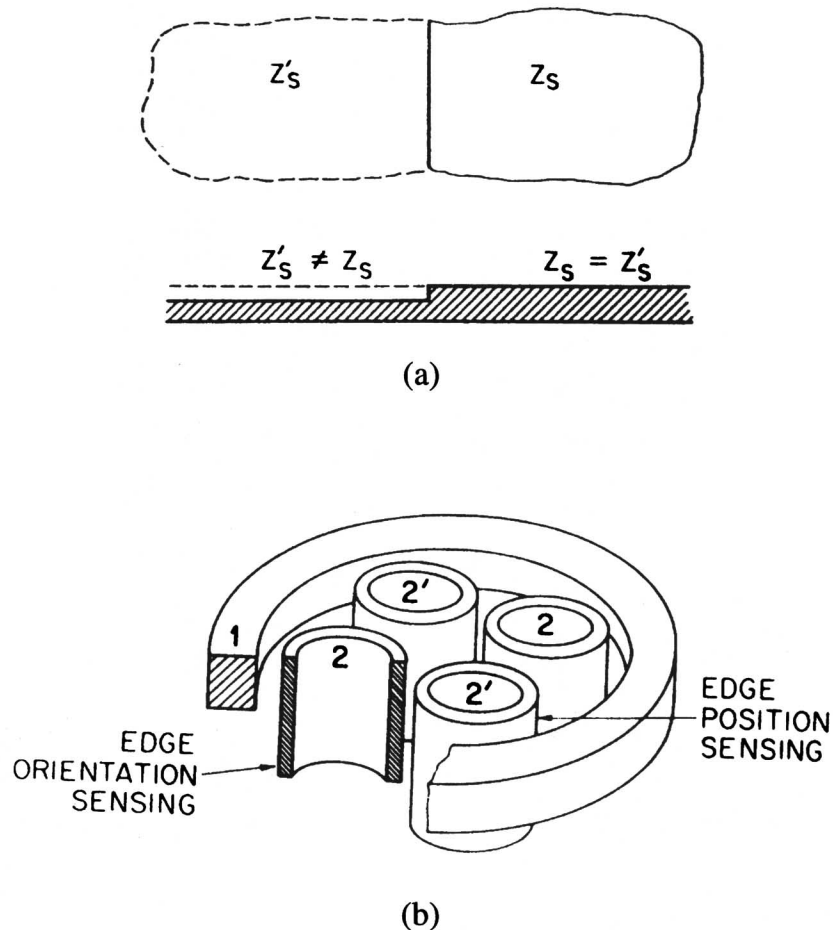

(a)

(b)

Fig. 7. Topographic sensor probe (after Ref. 109, with permission).

SCANNED PORTION OF SAMPLE

PARALLEL POLARIZATION   **PERPENDICULAR POLARIZATION**

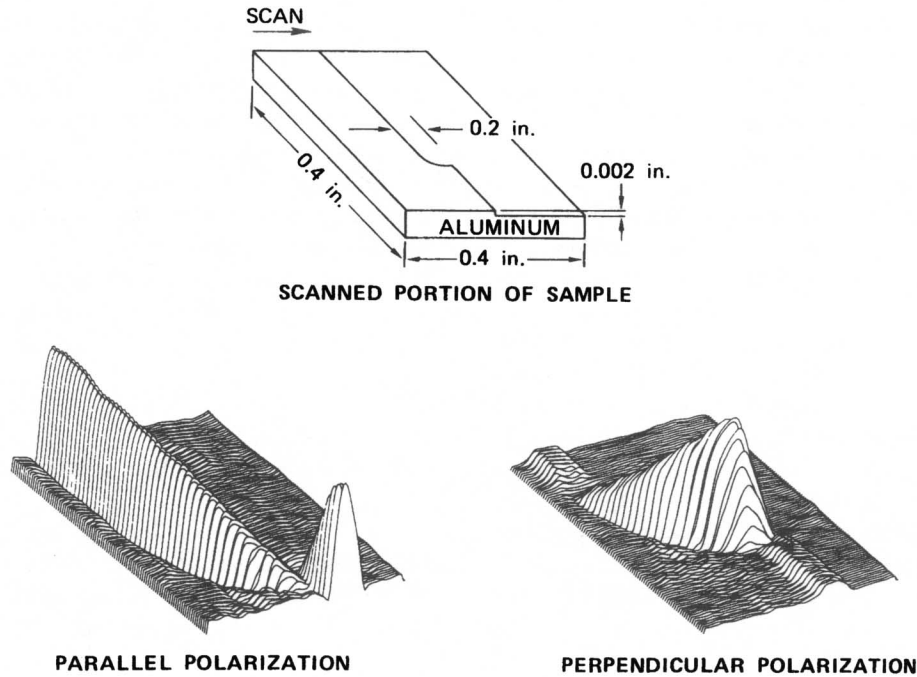**Fig. 8.** Response of a curved step (after Ref. 110, with permission).

of note with regard to edge and step modeling for topographical problems.

2.3.6. Liftoff, Tilt, and Material Characterization

Quasi-random variations of the liftoff distance l, where the cross-hatched region in Fig. 6 is an air gap, and of the tilt angle in Fig. 9[112] create a large "clutter" signal that can mask the defect signal during scanned probe measurements unless special precautions are taken.[113] Fixed probe measurements[112] and vertically scanned probe measurements, for material characterization, are also subject to errors due to inaccuracies in the liftoff and tilt positioning.

2.3.6.1. Analytical Methods. 2.3.6.1.1. Liftoff. The Fourier–Bessel[39–41] and angular Fourier[30,99,103] expansion methods described in Section 2.3.5 for layer problems are directly applicable to liftoff when the cross-hatched material layer in Fig. 6 is replaced by an air gap. The a-field evaluations for air-core coils of complicated shape in Refs. 9, 10, 13, 14, and 28 from Section 2.2.1 can be applied to two liftoff distances, using either (20), or the ΔZ relation (10a) and (10b) to evaluate the ΔZ due to the change in liftoff. Figure 10 shows the variations of the real and imaginary parts of ΔZ as a function of the liftoff distance z_0, with $l = 0$ in Fig. 6, and as a function of the testpiece skin depth. Traditionally scanned

defect responses ΔZ have been displayed as trajectory curves on the impedance plane illustrated in Fig. 10. Examples are given in Figs. 4 and 5 of Ref. 94. This display has the advantage of showing the angular difference in the impedance plane between the liftoff signal and the defect signal. By arranging the detection electronics to read only impedance plane variations perpendicular to the liftoff trajectory (Q axis in Fig. 10), the liftoff "clutter" signal can be minimized. Alternatively, the flaw profile display of the amplitude and phase of ΔZ as a function of a probe scan position along the plane of a crack—the flaw profile in Ref. 86 and Fig. 7 in Ref. 94 will be seen to be an especially convenient display for inversion. Details are given in Section 4.

2.3.6.1.2. Tilt. No analytical evaluations of the tilt effect have been made. Figure 11 illustrates a possible approach to this problem, by the angular spectrum method. The dashed line is a part of the surface of integration S_F in (10a). This surface is closed at a distance from the probe where the integrand becomes negligibly small.

2.3.6.1.3. Material Characterization. This topic has already been covered in Section 2.3.5.3.1, where it is shown in Fig. 10 that the angle of the liftoff trajectory depends on the material conductivity through the skin depth δ.

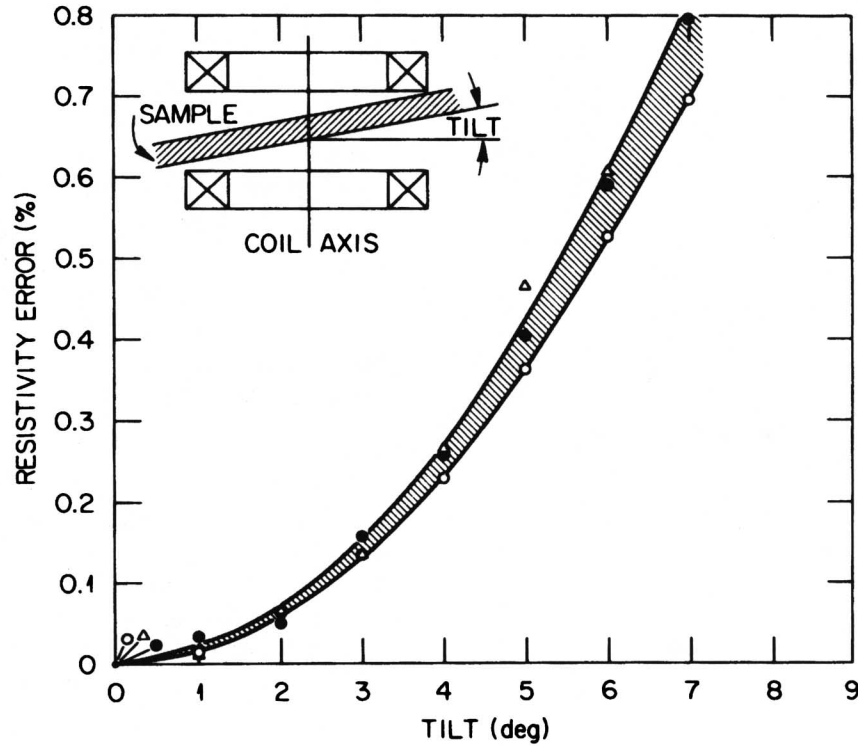*2.3.6.2. Numerical Methods.* All of the previously

Fig. 9. Errors due to probe tilt (after Ref. 112, with permission).

described numerical procedures are applicable to liftoff calculations, using either (20) or (10a) and (10b).

3. THE FORWARD PROBLEM

3.1. Probe–Defect Interaction

Analysis of probe–defect interactions in the thin skin approximation is demonstrated for a one-port probe and a surface-breaking crack or EDM notch. In (10a) the surface S_F, which can be any surface enclosing the crack, is first chosen to lie on the walls and mouth of the crack, as illustrated schematically in Fig. 5. Figure 5a shows the position of S_F in an unflawed testpiece. The a-field is calculated by one of the methods in Section 2.2, while the b-field is analyzed in the thin skin approximation. For an "almost-closed" surface-breaking crack this approach has been found to be in good agreement with experiments in nonmagnetic testpieces. Figure 5b illustrates the problem to be solved, a surface crack (or EDM notch) in a metal of finite conductivity. In an intermediate step the analysis treats the same crack in a perfectly conducting metal, shown in Fig. 5c.

A first approximation assumes that the tangential component of the magnetic field in the open mouth of the flaw (Fig. 5) is the same as at the same position on the surface of the unflawed metal (Fig. 5a). That is,

$$\hat{n} \times \vec{H}_A = \hat{n} \times \vec{H}_B = \hat{n} \times \vec{H}_C \qquad (37)$$

where capital subscripts are used to avoid confusion with a and b in (10a) and (16a). One argument in favor of this approximation is that an almost-closed surface flaw produces only a small perturbation of the magnetic field above the metal surface. This is in the same spirit as the Born approximation used for weak internal inclusions (25a) and (25b). Otherwise, the approximation may be considered as the first step in an iteration process, where the interior and exterior magnetic fields in and around the flaw are calculated in alternating steps.

On the parts of S_F that coincide with metal surfaces, the surface area M in Fig. 5a and the inner walls of the flaw in Figs. 5b and c, the boundary condition relating the magnetic field, which is tangential at the surface of a good conductor, to the tangential electric field is defined by the skin impedance. That is, for the A-, B-, and C-subscripted fields

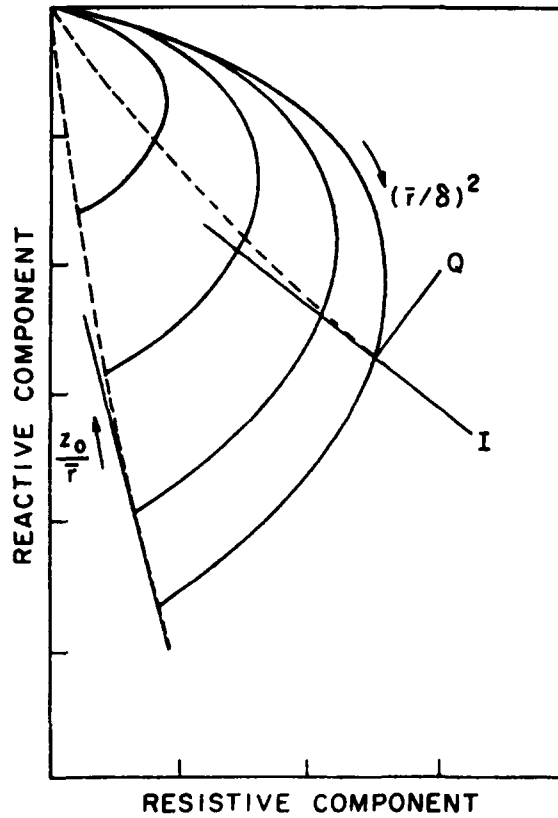$$\hat{n} \times \vec{E}_A = -Z_s \vec{H}_A \qquad (38a)$$

Fig. 10. "Comma" curves showing the variation of liftoff ΔZ with z_0 and δ (after Ref. 113).

Fig. 11. Schematic for evaluation of ΔZ from (10a) due to tilt, by the angular spectrum method (after Ref. 99).

same as if the walls were perfectly conducting (Fig. 5c). That is, the approximation

$$\vec{H}_C = \vec{H}_B \qquad \text{on and inside} \qquad S_F \qquad (39)$$

can be applied.

In summary, the fields under the integral in (10a) are obtained for the defect in Fig. 5b by first finding the magnetic field H_C inside the idealized defect of Fig. 5c, subject to the boundary condition (37) in the mouth of the flaw, and then approximating the B-subscripted magnetic field by (39). The tangential electric field E_B on the flaw walls is then obtained from (38b). In the mouth area M the B-subscripted electric field must be determined indirectly, as described below.

At this point it is convenient to enlarge the enclosing surface S_F so that it coincides with the surface of the flawed testpiece. On this surface the a- and b-subscripted E fields (in 10a) differ only on and near the crack mouth opening M. As a final approximation the integration is restricted to the crack mouth itself, reducing (10a) to

$$\Delta Z =$$

on M in Fig. 5a, and

$$\hat{n} \times \vec{E}_B = Z_s \vec{H}_B \qquad (38b)$$

$$\hat{n} \times \vec{E}_C = 0 \qquad (38c)$$

on the inner walls in Figs. 5b and c. [Recall that the normal vector $\hat{n}$ is directed toward the outside of S_F (Fig. 1). It is therefore directed away from the metal surface in (38a), but toward the metal surface in (38c).] The skin impedance in (38b) and (38c) is defined as

$$Z_s = \frac{1 + i}{\sigma \delta}$$

where σ is the metal conductivity, and δ is the skin depth as defined in Eq. (18). This is an approximation, using the skin impedance of a uniform plane surface and completely neglecting the disturbance of eddy current flow at the tip and edges of the defect. (These effects are considered in Section 3.3, below.)

The second approximation is based on the assumption of a highly conducting metal in Fig. 5b. In this case it can be shown, from microwave resonator theory,[2,3] that the magnetic field inside the flaw is essentially the
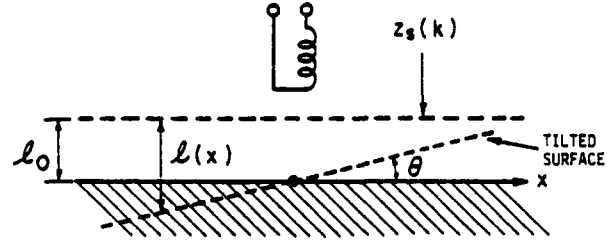
$$\frac{1}{I^2} \int_{\text{mouth}} (\vec{E}_a \times \vec{H}_b - \vec{E}_b \times \vec{H}_a) \cdot \hat{n} dS \equiv \delta_O - \delta_F \qquad (40)$$

where the first term represents the removal of a part of the unflawed surface and the second represents the addition of a defect. [A corresponding result for a two-port probe is obtained from (16a).] The first term in (40) can be reduced to

$$\delta_O = -\frac{1}{I^2} \int_{\text{mouth}} \vec{E}_a \cdot (\hat{n} \times \vec{H}_a) dS$$

$$= -\frac{Z_s}{I^2} \int_{\text{mouth}} \vec{H}_a \cdot \vec{H}_a \, dS \qquad (41)$$

by a vector triple product manipulation (Appendix B) and application of (37). The term on the right is obtained from the boundary condition (38a).

The next step is to convert the second term in (40) to a form in which the magnetic field solution of Fig. 5c can be used (Appendix C),

$$\delta_F = \frac{1}{I^2} \int_{\text{mouth}} \vec{E}_b \times \vec{H}_a \cdot \hat{n} dS$$

$$= \frac{1}{I^2} \int_{\text{mouth}} \vec{E}_b \times \vec{H}_C \cdot \hat{n} dS \tag{42a}$$

This substitution simplifies subsequent numerical evaluation of ΔZ. Since the Lorentz reciprocity relation (8a) applies to any two field solutions, it can also be written in terms of the B-subscripted and C-subscripted field solutions in Fig. 5 for all points inside S_F. Conversion to a surface integral by application of the divergence theorem then yields

$$\int_{\text{mouth \& walls}} (\vec{E}_C \times \vec{H}_B - \vec{E}_B \times \vec{H}_C) \cdot \hat{n} dS = 0 \tag{42b}$$

By vector triple product manipulation (Appendix C), the wall contribution in (42b) is converted to

$$\int_{\text{walls}} ((\hat{n} \times \vec{E}_C) \cdot \vec{H}_B - (\hat{n} \times \vec{E}_B) \cdot \vec{H}_C) dS = 0$$

The first term is zero from (38c). After substitution of (38b) and (39) the second term becomes

$$Z_s \int_{\text{walls}} \vec{H}_c \cdot \vec{H}_c dS$$

Combining these results in (42a) and (42b) and applying (37) yield the final result (Appendix B),

$$\delta_F = \frac{1}{I^2} \int_{\text{mouth}} \vec{E}_b \times \vec{H}_a \cdot \hat{n} dS$$

$$= \frac{1}{I^2} \int_{\text{mouth}} \vec{E}_C \times \vec{H}_C \cdot \hat{n} dS + Z_s \int_{\text{walls}} \vec{H}_C \cdot \vec{H}_c dS \tag{43}$$

Here the left-hand side is the total power delivered to the flaw, the first term on the right is stored energy inside the flaw, and the remaining term is dissipated power. Assembling (40), (41), and (43) then gives a general probe–defect interaction relation for almost-closed surface-breaking cracks and EDM notches.

3.2. Quasistatic Formulation

Since eddy current probes operate at very low frequencies, where the dimensions of the probe and of the defect are much smaller than a wavelength, the magnetic field H_C (Fig. 5c) in the interior of a surface-breaking defect can be represented by the gradient of a scalar potential. But note that for calculating the magnetic field outside the surface of the testpiece, where currents are present, the vector potential must be used. Calculation

of the magnetic field in (43) therefore reduces to a solution of a Laplace problem with well-defined boundary conditions. This can be carried out analytically for rectangular-shaped flaws, where a series solution for the interior magnetostatic problem can easily be obtained. This is not the case for the semielliptical shapes encountered in real fatigue cracks. For these geometries, the interior Laplace problem must be solved numerically, by either finite-difference or finite-element methods. In any case, it is convenient at this point to express (43) in quasistatic format using a scalar potential to represent the magnetic field in the interior of the flaw,

$$\vec{H}_C = \vec{\nabla}\phi \tag{44}$$

where ϕ is a solution to Laplace's equation satisfying (37) and the perfectly conducting wall boundary conditions in Fig. 5c. The following analysis originates with Refs. 84 and 85. Scalar potential modeling is also used by Beissner,[64,87] Burke,[86] and Hartfield and Bowler.[88] The extended scalar potential formulation by Nakagawa and Chao[82] puts the scalar potential method on a rigorous basis and renders it applicable to complicated geometries such as edges.[83]

The quantity integrated over the flaw mouth on the right side of (43) is zero on the flaw walls because, from Appendix C,

$$\vec{E}_C \times \vec{H}_C \cdot \hat{n} = \hat{n} \times \vec{E}_C \cdot \vec{H}_C$$

and this is zero on the walls (38c). Consequently, the integral can be extended over all of S_F, and the use of the divergence theorem yields

$$\int_{\text{mouth}} \vec{E}_C \times \vec{H}_C \cdot \hat{n} dS = \int_{S_F} \vec{E}_C \times \vec{H}_C \cdot \hat{n} dS \tag{45}$$

$$= \int_{V_F} \vec{\nabla} \cdot (\vec{E}_C \times \vec{H}_C) dV$$

In the quasistatic approximation (44) the volume integrand above can be written

$$\vec{\nabla} \cdot (\vec{E}_C \times \vec{\nabla}\phi) = \vec{\nabla}\phi \cdot \vec{\nabla} \times \vec{E}_C$$

$$= \vec{E}_C \cdot \vec{\nabla} \times \vec{\nabla}\phi$$

$$= \vec{\nabla}\phi \cdot \vec{\nabla} \times \vec{E}_C$$

since ϕ is a magnetic Laplacian potential. In the quasistatic regime, where (44) applies, the first approximation to $\vec{E}_C$ is given by the Faraday induction relation,

$$\vec{\nabla} \times \vec{E}_C = i\omega\mu_0 \vec{\nabla}\phi \tag{46}$$

and it follows that

$$\int_{\text{mouth}} \vec{E}_C \times \vec{H}_C \cdot \hat{n}dS = i\omega\mu_0 \int_{V_F} \vec{\nabla}\phi \cdot \vec{\nabla}\phi dV$$

in (43). Similarly, the second integral on the right side of (43) becomes, from (44),

$$\int_{\text{walls}} \vec{H}_C \cdot \vec{H}_C dS = \int_{\text{walls}} \vec{\nabla}\phi \cdot \vec{\nabla}\phi dS$$

Finally, in (40),

$$-\delta_F = -\frac{i\omega\mu_0}{I^2}\int_{V_F} \vec{\nabla}\phi \cdot \vec{\nabla}\phi dV$$

$$- \frac{Z_s}{I^2}\int_{\text{walls}} \vec{\nabla}\phi \cdot \vec{\nabla}\phi dS \qquad (47)$$

is expressed entirely in terms of the interior Laplace solution to the problem illustrated in Fig. 5c. In evaluating δ_O in (41) the field $\vec{\nabla}_a$ is obtained from the Dodd and Deeds vector potential calculation,[39-41] where the quasistatic approximation has already been applied. Combination of these results in (40) gives the final quasistatic formulation of ΔZ in terms of the unperturbed probe field in Fig. 5c and the interior Laplace potential in Fig. 5c. For an almost-closed surface crack δ_O is usually much smaller than δ_F and can often be neglected in a first approximation.

3.3. Crack Tip and Lip Correction Terms

Near the tip and lips of a surface-breaking crack, the eddy currents in the metal no longer flow parallel to the surface, as they do in a flat metal specimen. An analysis of this phenomenon carried out by Kahn[63,76] for a two-dimensional surface-breaking crack shows that the eddy current is concentrated where it flows around the tip of the crack and avoids the lips at the mouth of the crack. In other words, the current flow behaves like water flow around an obstacle. These changes in current distribution, which are localized over distances on the order of a skin depth, modify the wall integral contribution considered in (47).[84,85,88] In applying this two-dimensional analysis to the general problem above, the corrections given in the reference cited are weighted at each point on the crack periphery by the magnitude squared of the local magnetic field. In the quasistatic approximation the tip correction term is then given by

$$\delta_T = \frac{2.56}{I^2\sigma}\int_{\text{tip}} (\partial\phi/\partial\lambda)^2 \, d\lambda \qquad (48a)$$

and the crack lips correction is

$$\delta_E = \frac{1}{I^2\sigma}\int_{\text{edge}} (\partial\phi/\partial l)^2 \, dl \qquad (48b)$$

where λ extends along the crack tip and l along the crack lips. These correction terms are to be added to the right side of (40). Since the changes in eddy current distribution occur within a distance of several skin depths from the tip and the lips of the crack, it is clear that these correction terms become much smaller than δ_F for cracks whose dimensions are much larger than a skin depth.

3.4. Analytic Evaluation of ΔZ

The interior magnetic field is defined in the quasistatic approximation by (44), with

$$\nabla^2\phi = 0 \qquad (49a)$$

[Note that, according to the approximation (39), the interior magnetoquasistatic potential field for Fig. 5c is identical to the interior magnetostatic potential field for Fig. 5b.]

In the magnetoquasistatic approximation, the boundary condition (38c) is rewritten as

$$\hat{n} \cdot \vec{H}_C = 0$$

following the waveguide analysis in Ref. 3; and, in terms of the magnetostatic potential,

$$\frac{\partial\phi}{\partial n} = 0$$

on the inner walls of the surface-breaking crack. This can be restated as

$$\hat{n} \cdot \vec{\nabla}\phi = 0, \qquad \text{crack walls} \qquad (49b)$$

and in the mouth of the flaw, (37) requires that

$$\vec{\nabla}_T\phi = \vec{H}_T, \qquad \text{crack mouth area} \qquad (49c)$$

where the subscript T denotes a vector in the plane of the crack mouth. The field H_T can be obtained from the a-solution in Fig. 12.

To illustrate, consider the rectangular EDM model in Fig. 12a. This geometry is, in fact, a short-circuited rectangular waveguide that is below cutoff for all waveguide modes. When ω is far below cutoff the TE modes become magnetoquasistatic in nature[3] and constitute an orthogonal basis set for solving the problem at hand. The quasistatic modal solutions can be shown to be, from the reference cited and the boundary condition (49b),
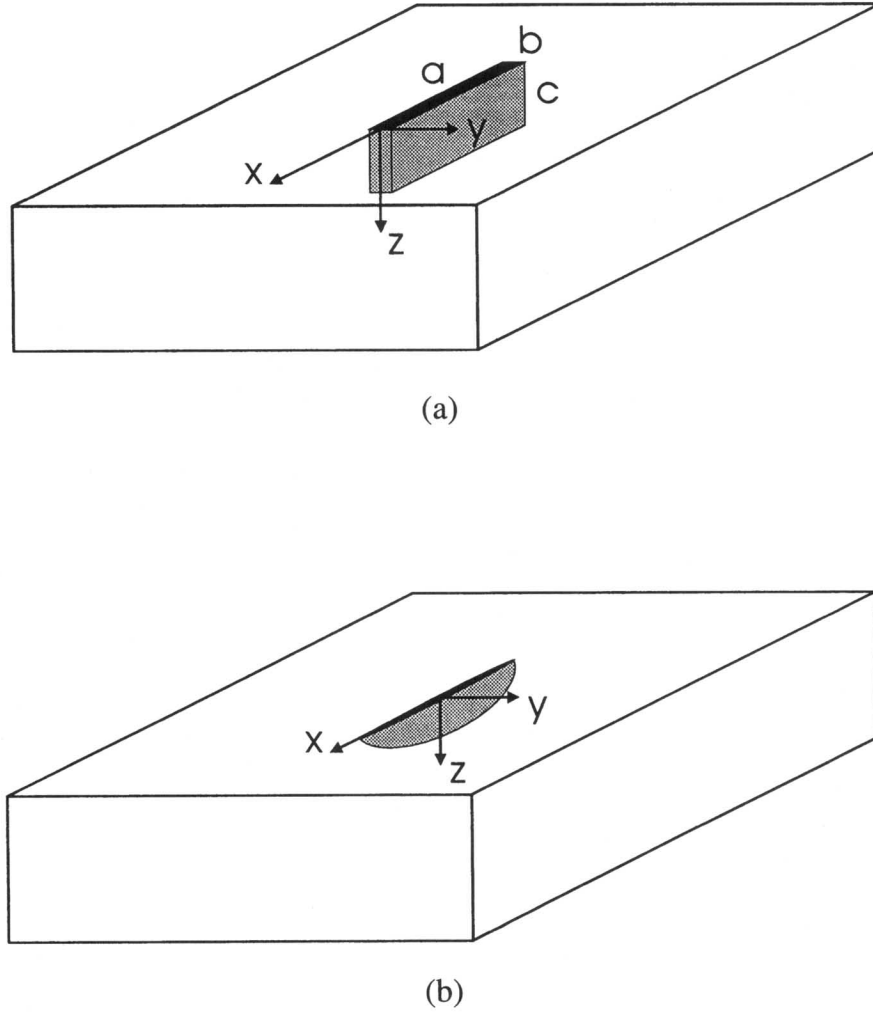
(a)

(b)

Fig. 12. Surface-breaking crack models. (a) Rectangular slot (EDM notch). (b) Semielliptical (or semicircular) slot.

$$\vec{H}_{mn}(x, y, z) = \hat{x} \frac{m\pi/a}{k_c} \cos \frac{m\pi x}{a} \sin \frac{n\pi y}{b} \cos k_c(z - c)$$

$$+ \hat{y} \frac{n\pi/b}{k_c} \sin \frac{m\pi x}{a} \cos \frac{n\pi y}{b} \cos k_c(z - c)$$

$$+ \hat{z} \cos \frac{m\pi x}{a} \cos \frac{n\pi y}{b} \sin k_c(z - c) \quad (50)$$

with

$$k_c = \left[\left(\frac{m\pi}{a}\right)^2 + \left(\frac{n\pi}{b}\right)^2\right]^{1/2}$$

These solutions satisfy the following orthogonality relation [3] in the mouth of the flaw,

$$\int_0^a dx \int_0^b dy \, \vec{H}_{Tmn}(x, y, 0) \cdot \vec{H}_{Tpq}(x, y, 0)$$

$$= \cos^2 k_c c \delta_{mn,pq} \quad (51)$$

where the subscript T denotes the transverse (or xy part) of the field.

The mode expansion for the transverse part of the interior field of the flaw can be written

$$\vec{\nabla}_T \phi = \vec{H}_T = \sum_{mn} a_{mn} \vec{H}_{Tmn} \quad (52a)$$

and, using the boundary condition (37), the expansion coefficients a_{mn} are obtained by applying the orthogonality condition (51). That is, from Ref. 3,

$$a_{mn} = \frac{1}{\cos^2 k_c c} \int_0^a dx \int_0^b dy \vec{H}_T(x, y, 0)$$

$$\cdot \vec{H}_{Tmn}(x, y, 0) \quad (52b)$$

The integral is evaluated using the a-solution in Fig. 12 to obtain H_T. The probe–crack interaction formula

$$\Delta Z = \delta_O - \delta_F + \delta_T + \delta_E \qquad (53)$$

is then evaluated by substituting (52) into (47) and (48).

This general three-dimensional formalism allows the crack to be placed either symmetrically (Fig. 13a) or asymmetrically (Fig. 13b) with respect to the probe. A scan of ΔZ versus probe position (crack profile) can be made either in the plane of the crack, as in the figure, or normal to the crack plane. The formalism can also be applied to very shallow open defects, or recesses, where the Born approximation (37) can again be applied, justified by the fact that the defect is very shallow.

3.5 Numerical Evaluation of ΔZ

For semicircular and semielliptical slot geometries (Fig. 12b), the ΔZ formula cannot be easily evaluated by an analytical approach. In such cases Δz was first evaluated by the finite-difference method.[20,91] Only the case of an almost-closed crack, with the probe centered over the plane of the crack and scanned in the plane of the crack Fig. 13a, is considered here. The fields and potentials are, in this case, approximately uniform across the flaw opening, and the three-dimensional (x, y, z) problem detailed in Section 3.1 can be reduced to a two-dimensional (x, z) problem. In applying the method it is useful to manipulate (47) so that only one integral is involved. First, it is noted that for the two-dimensional problem the wall integral in (47) is twice the integral over one wall. Furthermore, the volume integral is the integral over one wall multiplied by the crack opening Δu,

$$\int_{V_F} \vec{\nabla}\phi \cdot \vec{\nabla}\phi dV = \Delta u \int_{one\ wall} \vec{\nabla}\phi \cdot \vec{\nabla}\phi dS \qquad (54)$$

This relation reduces (47) to

$$\delta_F = -\frac{i\omega\mu_0\Delta u + 2Z_s}{I^2} \int_{one\ wall} \vec{\nabla}\phi \cdot \vec{\nabla}\phi dS \qquad (55)$$

The analytical approach in Section 3.4 is applied to the rectangular two-dimensional problem by taking the mode index n to be zero in (52a), which restricts the field expansion to modes that are uniform across the dimension $b = \Delta u$ of the crack (Fig. 13a).

For numerical evaluation of the two-dimensional problem, it is convenient to convert the wall integral of (55) into an integral over the flaw mouth. From Green's theorem and (49a)

$$\vec{\nabla} \cdot (\phi\vec{\nabla}\phi) = \vec{\nabla}\phi \cdot \vec{\nabla}\phi + \phi\nabla^2\phi = \vec{\nabla}\phi \cdot \vec{\nabla}\phi$$

An integration over the interior volume of the flaw and application of the divergence theorem yields

$$\int_{V_F} \vec{\nabla}\phi \cdot \vec{\nabla}\phi dV = \int_{V_F} \vec{\nabla} \cdot (\phi\vec{\nabla}\phi)dV$$
$$= \int_{walls\ \&\ mouth} \phi\frac{\partial\phi}{\partial n}dS \qquad (56a)$$

From (49b) the right-hand integrand in (56a) is nonzero only over the mouth, and substituting from (54) yields

$$\int_{one\ wall} \vec{\nabla}\phi \cdot \vec{\nabla}\phi dS = \frac{1}{\Delta u}\int_{mouth} \phi \frac{\partial\phi}{\partial n} dS \qquad (56b)$$

Then (55) becomes

$$-\delta_F = \frac{i\omega\mu_0\Delta u + 2Z_s}{I^2}\frac{1}{\Delta u}\int_{mouth} \phi\frac{\partial\phi}{\partial n}dS \qquad (57)$$

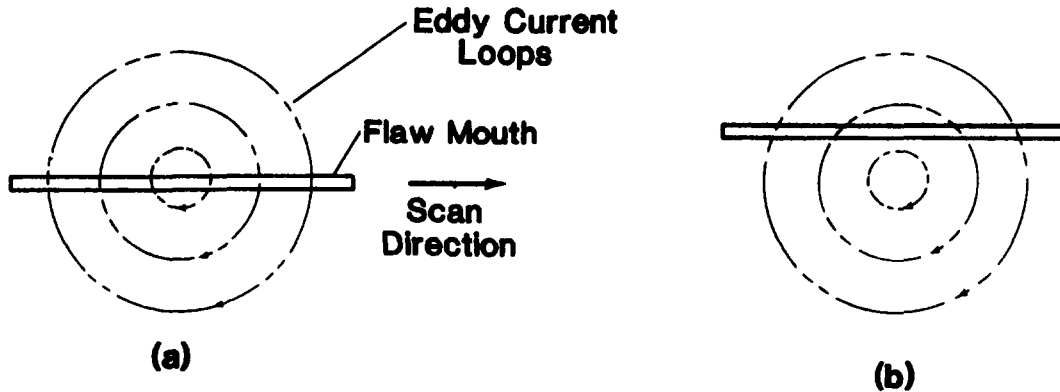**Fig. 13.** Defect profile scans. (a) Symmetric. (b) Asymmetric.

When ϕ and $(\partial\phi/\partial n)$ are approximated as uniform across the opening, the right-hand integral (Fig. 13a) in (57) becomes

$$\int_{mouth} \phi\frac{\partial\phi}{\partial n}dS = \int_{-b/2}^{b/2} dy \int_{-c/2}^{c/2} dx\,\phi\frac{\partial\phi}{\partial n}$$
$$= \Delta u \int_{-c/2}^{c/2} \phi\frac{\partial\phi}{\partial n}dx \qquad (58)$$

where the Δu in (58) cancels the Δu [in (57)].

The potential function boundary condition in the mouth of the flaw is defined by the unperturbed interrogating field of the probe, from (37), and integration of (49c). It is clear from (55) that ΔZ is independent of the arbitrary constant of integration. The wall boundary condition (49b) completes the statement of the interior potential problem. Finite-difference solutions[20,91] are generated numerically by starting with a coarse finite-difference mesh and then successively refining the mesh size until the desired convergence is obtained. In this procedure new mesh values were obtained from the old values and interpolation.

Special care must be taken in applying boundary conditions on a semicircular or semielliptical boundary.[91] Starting from a rectangular mesh, nodes are defined as exterior, interior, or border points. Exterior points are ignored, while interior points are treated by a standard fourth-order approximation. Exterior points are ignored, while interior points are treated by a standard fourth-order approximation. Border points are categorized using geometric relationships relative to the boundary. In the iteration procedure pointwise successive relaxation is used, automatically adjusting the overrelaxation parameter to avoid divergence. From the interated solution the normal derivative required in (57) is calculated numerically and the integration along the flaw mouth is carried out numerically by Simpson's rule for unequal intervals. The singularities of the normal derivative at the ends of the flaw cause some slowing of the convergence, but this is not a serious problem.

Comparisons of experiment and theory in[20,80,91] provide an empirical justification for assuming ϕ and $(\partial\phi/\partial n)$ to be uniform across Δu for almost-closed surface breaking defects.

The above numerical evaluation of probe response to a symmetrically scanned surface breaking crack (Fig. 13a) generate a flaw profile (Fig. 14) that directly indexes the ends of the crack. Figure 14 clearly shows the physical reason for this behavior and illustrates the importance of
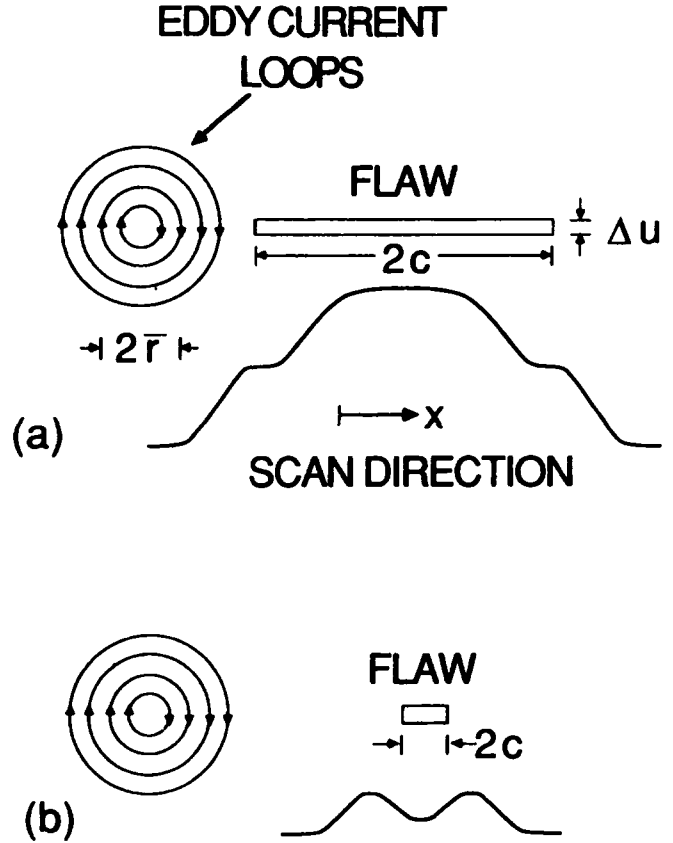

Fig. 14. Schematic representations of defect profile curves. (a) Small probe diameter. (b) Large probe diameter. (After Ref. 80, with permission.)

properly choosing the probe diameter. Dashed circles indicate the position of the probe coil and the eddy current vortexes in the test piece under the coil.

In Fig. 14a small flat spots appear in the profile when the center of the vortex is over one end of the crack. The reason is that the eddy current strength goes to zero at the vortex center, so that the probe signal does not change for small probe displacements near the end of the crack. In Fig. 14b, where the crack length is much smaller than the probe diameter, the flat spots do not appear. The flaw profile scan then simply displays the squared profile of the probe field distribution.

As noted in Section 2.2.1 the depth of penetration of the probe field into the substrate is related to skin depth in the thin skin limit and to the coil diameter in the thick skin limit.[42] These features must be kept in mind when applying the flaw profile method to defect characterization.

4. INVERSION

4.1. Mathematical Inversion, Imaging, Defect Reconstruction, and Defect Characterization

General eddy current inspection for defects comprises three functional steps: detection, location, and description. The third step is very commonly termed defect sizing. In the forward problem ΔZ of the probe is analyzed for a particular type of defect in a particular location, as a function of the scanned position of the probe. In the inverse problem, the aim is to determine the nature and location of a defect from the scanned ΔZ data output of the probe.

In early eddy current practice (Chapters 2 and 5 in Ref. 4) the approach was qualitative and empirical, using equivalent circuit conceptual models and experimental simulated defect models, fabricated to varying degrees of realism. Recorded data were displayed in the impedance plane format (Fig. 10) for phase discrimination against the time varying liftoff signal generated by a hand-held probe scan. The nature of a defect was deduced by comparing the impedance plane trajectory for the defect with impedance plane trajectories for a selection of simulated defects. In other words, the identification procedure was a qualitative and subjective form of pattern recognition. But even at the time (1965) the need for a more quantitative approach was recognized (Chap. 10 in Ref. 4).

Programs of research targeted to quantitative nondestructive evaluation were first initiated in the 1970s, leading to the organization of a series of annual conferences devoted to the subject and beginning publication in 1982 of Volume 1 in the series of annual bound conference proceedings, *Review of Progress in Quantitative NDE*. For eddy current NDE a rapid increase in the sophistication of modeling and experimental techniques resulted. As analytical and numerical models evolved, it became possible to reconstruct defect geometries by fitting recorded ΔZ data with computed ΔZ data for assumed types of defects. This defect reconstruction procedure is now widely practiced. Improved mechanical scanners and electronic instrumentation provide an extensive choice of ΔZ data display modes, including two-dimensional scanned amplitude and phase images that permit classification of defects into their particular categories as required for implementation of inversion procedures.

Inversion of the system of governing equations for the interaction of the probe with a defect has been performed rigorously (mathematical inversion) for some special problems that satisfy the required invertibility and uniqueness conditions. These conditions are more severe for eddy current, rather than optical problems, because

of the extreme degree of attenuation in an eddy current medium. But it should be noted that the principles of geometric optics have long been applied to dissipative media[115] so that it is logical to speak of eddy current imaging, first demonstrated by Copley[116] as a means to classify partially defects as to type (cracks, voids, etc.). The diffusion equation governing eddy current behavior is, in fact, the limit case of the dissipative wave equation when the losses become very large.[117] However, in eddy current imaging, the complicated geometric shapes of the object (defect) and the source (probe), as well as the very large material losses and interface reflections, lead to very severe imaging aberrations. The result is that the image does not closely resemble the object. Various image processing and restoration techniques have been applied to the problem, including what is commonly termed eddy current holography.[118,119] Holographic (or "complete") recording was developed in optics as a means for recording both amplitude and phase information as amplitude-only information, permitting restoration of a three-dimensional image. In the eddy current case, the very severe attenuation of the medium requires certain modifications of the technique, including use of an electronically injected phase reference signal rather than the phase reference beam used in optics. The phase of the recorded ΔZ data, which encompasses a very limited range, is also augmented (or multiplied) electronically. For these reasons it may be reasonable to use the term "phasography"[120] to distinguish the eddy current technique from that used in optics.

The following lists selected references to illustrate the details of commonly used inversion procedures.

4.1.1. Mathematical Inversion

In Ref. 121 a direct linear inverse method is presented for eddy current measurement of three-dimensional conductivity measurements. The form of the probe is a spatially periodic current sheet. It is supposed that the conductivity variations are small so that the Born approximation (25a) and (25b) may be used, thereby linearizing the inversion equations. Inversion of the three-dimensional problem requires inversion of a coupled Fourier–Laplace transform. In one-dimension, the depth and conductivity of coatings may be reconstructed exactly from the inverse Born profiles. Reference 122 uses the same probe structure to obtain by inversion, in the asymptotic low-frequency limit, the exact dc conductivity of a surface layer on a substrate of Ref. 85 of different conductivity.

4.1.2. Imaging

Reference 116 first introduced the practice of using imaging to categorize quickly a defect according to its general type. An electromagnetic model for eddy current imaging, based on use of the ΔZ relations, was later used to compare optical and eddy current imaging systems with regard to aberrations, point spread functions, and the choice of image processing techniques.[123] In Ref. 124 image restoration was formulated as a maximum-likelihood estimation problem, treated by constrained iterative gradient descent. Synthetic images of a number of defect configurations were created. Eddy current holography (or phasography) using phase reference multiplication to overcome the problem of small eddy current penetration and to achieve adequate resolution was discussed in Refs. 118 and 119. Imaging with eddy current arrays was reviewed in Ref.37, where the advantages of comprehensive array generated data sets were compared with traditional impedance plane Lissajous patterns from a single line scan.

4.1.3. Reconstruction

Image restoration in Section 4.1.2 was concerned with maximizing the information content of the two-dimensional image recorded by the probe and with improving the sharpness and resolution of the detail. Defect reconstruction, in contrast, deals with estimation of the defect's boundary shape (crack, pit, void, etc.) or the spatial distribution of conductivity changes (inclusions, layers, etc.). The procedure used is to minimize the error between the measured data and the data produced from a field model of the probe–defect interaction, by varying the defect parameters. Details of the minimization procedure vary among the references cited. Some treatments chose a more restricted range of defect parameters than others.

In Refs. 84 and 85 the model used is the thin skin model and the defect is a rectangular slot, while Refs. 125 and 126 present a numerical method applicable to two- and three-dimensional conductivity distributions, following contemporary work in electromagnetic and geophysical inversion. Reference 127 begins with a brief general discussion of the eddy current inversion problem and then formulates the problem of a surface-breaking crack as a parameter estimation problem using a finite-element model of the forward problem. The same defect geometry is treated in Ref.128 in the context of the acfm technique,[13] but the method is also applicable to a related eddy current technique (79). In Ref. 128, the forward model is based on the "unfolding" technique,[78] involving

solution of a two-dimensional Laplace analysis for the crack interior. The problem is solved for a crack of general shape using the boundary-element method. The forward model in Section 3 also represents the interior field of the crack in terms of a two-dimensional Laplace potential (magnetostatic, in this case), so that the same inversion procedure[128] may again be adopted, using the boundary-element method and iteration.

A very different approach is followed in Ref.110 for the problem of reconstructing electrical conductivity profile distributions. Variable frequency data, with varying penetration depths, make it possible to recover the conductivity as a function of depth. Reference 129 describes an iterative least-squares method for inverting eddy current probe impedance data, based on analytically formulating the spatial gradient of the scanned probe impedance data. An important feature is that this result is independent of the type of numerical discretization used. Examples of a layer problem and an ellipsoidal crack are given. In Ref. 130, the impedance gradient approach is applied to the inversion of flaw profile data[91] for both semielliptical and irregular cracks. Reference 131 presents a defect reconstruction procedure based on the forward model in Section 3, for a long crack of uniform depth and opening, following the thin skin treatment of an infinite (two-dimensional) crack.[85] The inversion procedure performs a least-squares polynomial fitting of the data. Use of eddy current arrays for defect reconstruction has been treated in detail in Ref. 37. Arrays have the useful feature that data may be taken with variable geometry arrays[35] to acquire a more complete database. In Ref. 37 three-dimensional reconstruction is discussed and the relation of this procedure to the restoration of the defect's two-dimensional top view is analyzed.

4.1.4. Characterization

Defect characterization is defined here as the procedure that estimates some of a defect's parameters by matching certain features of the experimental and model data sets, rather than by performing an iterative least-squares fitting of the complete data sets, as in reconstruction. This approach relies heavily on physical insight and visual selection of the features to be matched and the parameters to be characterized. The result is a rapid and efficient procedure, realized at the cost of a reduced information output concerning the geometrical shape of the defect. Reference 85 considers procedures that share to some extent the reconstruction and characterization approaches to the problems of rectangular surface-breaking cracks and slots. In Refs. 80, 131, and 91 the length, depth, and opening of rectangular and semielliptical sur-

face-breaking defects are estimated. The procedure is based on flaw profile data (Fig. 14) and the sensitivity of depth data to the diameter of the probe (Section 2.3.2). Another approach to defect characterization, in Ref. 127, works from data sets consisting of Lissajous trajectories in the impedance plane data display mode (Fig. 10). The technique relies on a Fourier descriptor mapping to extract and compress the data into a reduced set of signature (or feature) parameters so as to reduce computational effort and improve performance of the classification procedure.

Inversion of eddy current data from homogeneous and inhomogeneous surface layers has attracted increased attention in recent years. Reference 133 treats the problem of determining the thickness and conductivity of a uniform layer, while Ref. 134 solves the forward problem for a nonuniform layer. In Ref. 135 a feature-based procedure for rapid inversion of layer thickness and conductivity is described. Reference 136 gives a preliminary report on pulsed eddy current characterization of corrosion layers. As a result of recent advances in electronic instrumentation the quality of pulsed eddy current measurements has substantially improved. Time-domain displays permit new approaches to inversion and provide improved lift-off discrimination.

4.2. Surface-Breaking Cracks and Slots

There is now a growing trend in eddy current practice toward assembling sets of benchmark defect simulations, together with corresponding analytical and numerical models.[86,94,137] These simulations and models are used as were those described in Ref. 4 but for much more complicated geometries and much more sophisticated theoretical models. They are also applied as forward solutions for defect reconstruction procedures.

4.2.1. Reconstruction

The forward problem for an ideal crack of arbitrary shape is solved in Ref. 69 by the boundary element method with an exact formulation of the electromagnetic Green's function. Reference 130 applies this forward solution to an iterated minimization of the difference between estimated ΔZ and measured ΔZ. The procedure uses a descent algorithm requiring knowledge of the gradient of the error with respect to a variation of the crack geometry. The boundary-element method is well adapted to this kind of problem because it easily adapts to problems with irregularly shaped crack boundaries.

Figure 15 illustrates a general inversion performed by this technique. Following the example of Ref. 127, this lengthy inversion procedure could be shortened by using the approximate scalar potential model in Section 3.

4.2.2. Characterization

The inversion process can be further accelerated by matching only a finite number of flaw profile features. From the flaw profile in Fig. 14 the length c of the crack can be obtained visually. The crack depth a and crack opening Δu can be obtained from the amplitude and phase of ΔZ at the center point of the crack. It is found empirically that the amplitude and phase data, when plotted as in Fig. 16 for a known crack length c and skin depth δ, exhibit contours of constant a and constant Δu that are nearly orthogonal. Consequently, these parameters can be estimated from the measured amplitude and phase coordinates. It should be noted in Fig. 16 that, as predicted in Section 2.3.2, the method breaks down when the crack depth a is much greater than the probe radius $\bar{r}$ (normalized to a).

4.3. Layers

4.3.1. Frequency-Domain Inversion

In Ref. 129 a layered conductor with unknown layer conductivities is treated as a test of the reconstruction procedure. But for a single unknown layer the characterization procedure in Ref. 135 is more efficient.
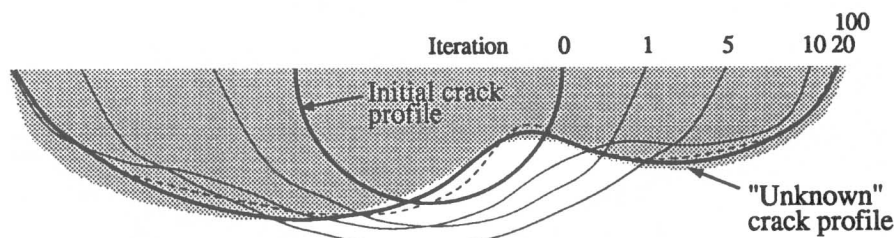

Fig. 15. Inversion by iteration of an irregular crack. The profile after 20 iterations is dashed; that after 100 iterations is bold. (After Ref. 129, with permission.)
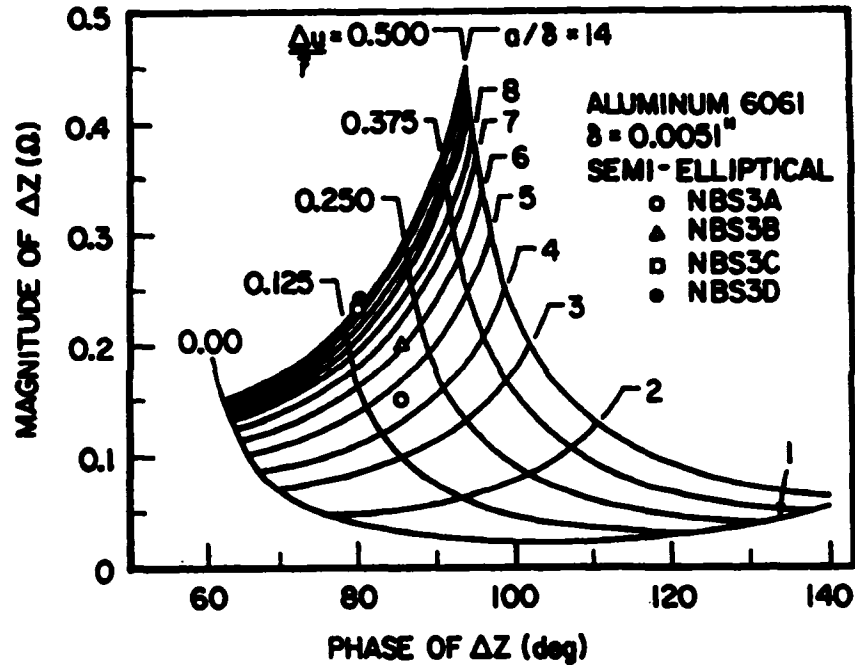
Fig. 16. Quasi-orthogonal contours of crack depth a and opening Δu, in the magnitude-phase plane—McFettridge chart (after Ref. 131).

4.3.2. Time-Domain Inversion

Reference 136 demonstrated the characterization of a multilayer model of corrosion in aircraft skin splices, proving the efficiency of this procedure. It should be noted again that, because of the time delay of the probe response, the sensitivity to liftoff is very substantially reduced for time domain operation. In the reference cited, standard probe coils (air and ferrite core) were used and the time-domain signal was obtained from the frequency-domain signal by a Fourier transform. Figure 17 illustrates the raw experimental data and the inverted results.

Modeling of probe fields specialized to the optimization of the probe–defect interaction and interpretation of the forward problem response has received some attention. Reference 138 considered optimized probe design, working directly in the time domain, while Ref. 139 considered the probe–defect interaction. The second reference worked directly with the time domain version of the reciprocity relation, applied to a two-dimensional surface crack interrogated by a plane wave.

4.4. $\Delta\Gamma$ (or ΔS) Relations

The three pulsed eddy current references[136,138,139] cited above considered either a simplified defect structure (layers) or a simplified interrogation field (plane wave). But recent advances in pulsed eddy current technology, coupled with corresponding successes in defect detection,

motivate a search for commensurate improvements in modeling methods. The time-domain character of pulsed eddy current testing has not yet been fully exploited with regard to both the forward and the inverse problems.

It is highly desirable to begin searching for a time-domain modeling methodology with a flexibility and completeness comparable to that of the ΔZ frequency-domain approach reviewed in this paper. In pulsed eddy current measurements the attenuation in the test piece is large, and the time delay is small. The result is that changes in voltage at the probe terminals contain strongly overlapping reflected and incident pulses. This masks the crucial defect information contained in the waveform of the reflected pulses.

All of this suggests that one can profit by choosing $\Delta\Gamma$ (the change in reflection coefficient at the probe terminals), rather than ΔZ, as the defect parameter of primary interest. This choice is reinforced by the fact that low-frequency directional couplers to separate the reflected wave from the incident wave are readily available in the form of suitably designed bridge circuits.

To model the performance of a one-port pulsed eddy current system, there exists a reciprocity-based $\Delta\Gamma$ relation of similar form that that of the ΔZ relation. From Ref. 6,

$$\Delta\Gamma(\omega) = \frac{1}{4P} \int_{S_F} (\vec{E} \times \vec{H}' - \vec{E}' \times \vec{H}) \cdot \hat{n} dS \quad (59)$$
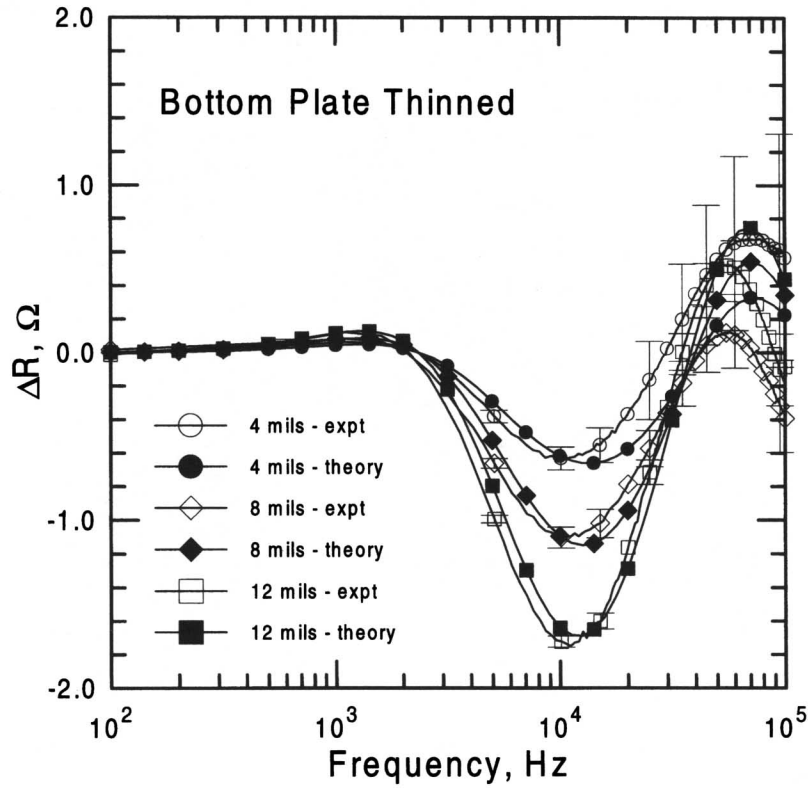
Fig. 17. Pulsed eddy current inversion of the thickness dimensions of a two-plate structure with an air gap. (a) Time-domain data. (b) Dimensional characterization.

where P is the power in the incident wave, and the evaluation is performed in the frequency domain. The change in the frequency spectrum of the reflected pulse is obtained by multiplying (59) by the frequency spectrum of the incident pulse. Fourier transform of the result gives the change in the time-domain wave form of the reflected pulse, due to the presence of a defect.

The integral in (59) is of exactly the same form as the ΔZ, when subscript a is appended to the unprimed field quantities and subscript b to the primed field quantities. Therefore, all of the modeling techniques developed for ΔZ are again applicable. Since pulsed eddy current probes are customarily two-port, rather than one-port, the required two-port variant of (59) can be obtained by following the procedure in Section 2.1.2. This yields changes in the elements of the reflection–transmission coefficient matrix, *i.e.*, $\Delta \Gamma_{11}$, $\Delta \Gamma_{12} = \Delta \Gamma_{21}$ and $\Delta \Gamma_{22}$. When P is normalized to unity at both ports, $\Delta \Gamma_{11}$, etc., represent changes ΔS_{11}, etc., in elements of the scattering matrix for the two-port probe.

With this information, all of the modeling methods applied to ΔZ in the frequency domain become applicable to $\Delta \Gamma$ in the time domain.

5. SUMMARY

A full derivation has been presented for a set of ΔZ relations that express in a unified format the response of an arbitrary (one-port, two-port, array) eddy current probe to an arbitrary defect. This result is given as an integral over the region of the defect, with the integrand expressed in terms of the defect parameters (shape, material properties, etc.) and the probe field distribution in the vicinity of the defect both in the absence (a-field) and in the presence (b-field) of the defect. The probe response is in the frequency domain, but can be converted to the time domain for pulsed eddy current applications[135] by taking Fourier transform.
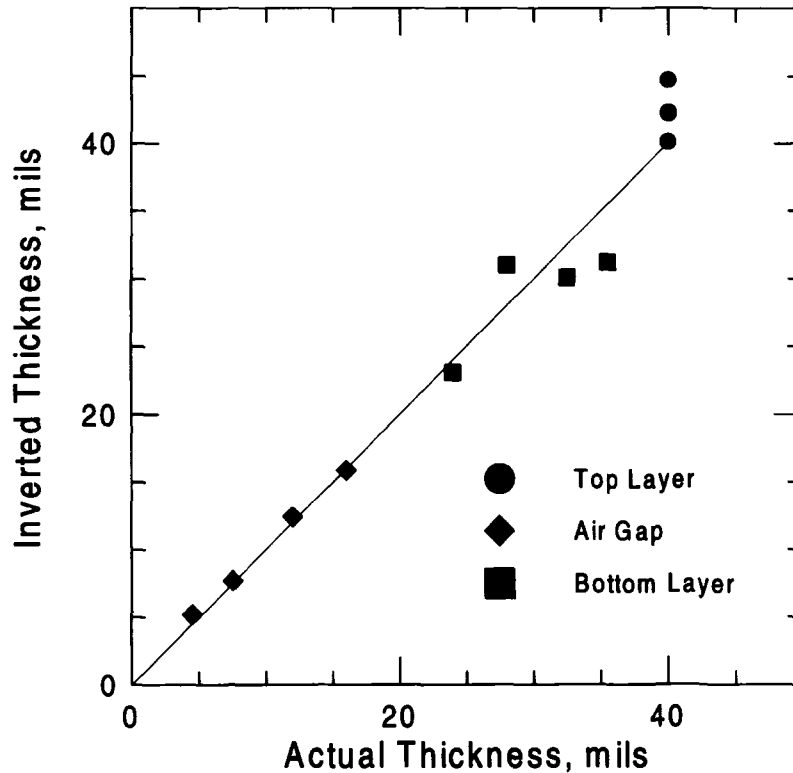
(b)

Fig. 17. *Continued*

The ΔZ format is applicable to any eddy current modeling problem and requires only calculation of the a- and b-fields, by either analytical or numerical means. This permits treatment of classes of similar defects in a unified way. Restriction of the integral to the vicinity of the defect (the "localization" property) improves the precision of numerical evaluations of small ΔZ signals by calculating ΔZ directly rather than taking the small difference between the much larger probe impedances Z_b and Z_a. Furthermore, the ΔZ format reduces the computational load in numerical evaluations by restricting the discretization to a small region around the defect. And, finally, by focusing on the region of the defect, the ΔZ formulation fosters improved physical insight and the development of analytical approximations.

References cited give examples of a-field and b-field calculations, both analytical and numerical, for a wide variety of probes and defects. Emphasis is placed on physical interpretations wherever possible. The specific example of a surface-breaking crack or notch is chosen to illustrate solution of the forward problem in the thin

skin approximation and to introduce the importance of the mode of data display (impedance plane, flaw profile, image, phasography, etc.) with regard to defect feature classification, optimization by signal processing, and suppression of liftoff clutter. A brief review of inversion procedures is given, with a selection of reference examples.

An alternative approach to reciprocity-based modeling using $\Delta\Gamma$ (or ΔS) relations has also been introduced. These relations lead to expressions for changes in the reflection–transmission (or scattering) coefficients of a probe, due to the presence of a defect. These quantities are given in terms of localized integrals over the region of the defect. Although they are calculated in the frequency domain, these scattering coefficients may be used to evaluate *in the time domain* changes in the reflected and transmitted pulses generated by the presence of a defect. Such a formulation of the pulsed eddy current problem retains all of the advantages of the ΔZ method reviewed above, while operating in the time domain. It therefore promises to motivate the development of sophisticated

approaches to modeling and inversion in pulse-based eddy current NDE.

Future trends in eddy current testing emphasize a rapid evolution of new probe technology (arrays for rapid scanning, SQUID detectors for increased material preparation, etc.), a continuing development of sophisticated modeling for complex geometries, and some continuing extension into the high-frequency and microwave domains.

APPENDIX A

As $R \to \infty$, the a-field and the b-field in (8b) can be expressed as superpositions of outgoing spherical modes,[8]

$$\vec{H}_a = \sum_n A_n^a \vec{h}_n(r, \theta, \phi), \quad \vec{E}_a = \sum_n A_n^a \vec{e}_n(r, \theta, \phi) \quad (A1)$$

and

$$\vec{H}_b = \sum_n A_n^b \vec{h}_n(r, \theta, \phi), \quad \vec{E}_b = \sum_n A_n^b \vec{e}_n(r, \theta, \phi) \quad (A2)$$

Because the spherical modes are orthogonal over the surface of the sphere,[3] substitution of (A1) and (A2) into the left side of (8b) yields

$$\sum_n A_n^a A_n^b \oint_s (\vec{e}_n \times \vec{h}_n - \vec{e}_n \times \vec{h}_n) \cdot d\vec{s} = 0$$

so that the contribution of the enclosing infinite sphere vanishes.

APPENDIX B

In (10a) the surface S_F enclosing the defect in Fig. 1 can be chosen in a variety of ways, depending on the shape of the defect. In Section 2.2 this is demonstrated for the case of a surface-breaking crack. For defects such as inclusions and voids, it is convenient to express ΔZ as a volume integral rather than a surface integral. This is accomplished by first using the divergence theorem to write (10a) as

$$\Delta Z = \frac{1}{I^2} \int_{V_F} \vec{\nabla} \cdot [\vec{E}_a \times \vec{H}_b - \vec{E}_b \times \vec{H}_a] dV \quad (B1)$$

where V_F is the volume enclosed by S_F in Fig. 1. Using the identity

$$\vec{\nabla} \cdot (\vec{A} \times \vec{B}) = \vec{B} \cdot \vec{\nabla} \times \vec{A} - \vec{A} \cdot \vec{\nabla} \times \vec{B} \quad (B2)$$

and Maxwell's equations, (B1) can be converted to the volume integral format (10b). In the case of an inclusion

or a void it is convenient to shrink the surface S_F around the defect, so that V_F becomes the volume of the inclusion or void.

APPENDIX C

Applying the vector triple product identity

$$\vec{A} \cdot (\vec{B} \times \vec{C}) = \vec{B} \cdot (\vec{C} \times \vec{A}) = \vec{C} \cdot (\vec{A} \times \vec{B}) \quad (C1)$$

to the first term in the integrand of (40), with $\vec{C} = \hat{n}$, yields

$$(\vec{E}_a \times \vec{H}_b) \cdot \hat{n} = \hat{n} \cdot (\vec{E}_a \times \vec{H}_b) = \vec{H}_b \cdot (\hat{n} \times \vec{E}_a) \quad (C2)$$

Application of (38a) and (37) reduces this result to

$$-Z_s \vec{H}_b \cdot \vec{H}_a = -Z_s \vec{H}_a \cdot \vec{H}_a \quad (C3)$$

which generates (41).

The integrand of the first member in (42a) can be converted as follows, using (B1) and (37):

$$(\vec{E}_b \times \vec{H}_a) \cdot \hat{n} = \vec{E}_b \cdot (\vec{H}_a \times \hat{n})$$
$$= \vec{E}_b \cdot (\vec{H}_c \times \hat{n}) \quad (C4)$$
$$= (\vec{E}_b \times \vec{H}_c) \cdot \hat{n}$$

From (C.1), again,

$$(\vec{E}_c \times \vec{H}_b) \cdot \hat{n} = (\hat{n} \times \vec{E}_c) \cdot \vec{H}_b \quad (C5)$$

and

$$-(\vec{E}_b \times \vec{H}_c) \cdot \hat{n} = -(\hat{n} \times \vec{E}_b) \cdot \vec{H}_c \quad (C6)$$

in the integrand of (42b).

To obtain (43), note from (42a) and (42b) that

$$\int_{mouth} (\vec{E}_b \times \vec{H}_c) \cdot \hat{n} dS = \int_{mouth} (\vec{E}_c \times \vec{H}_b)$$
$$\cdot \hat{n} dS + Z_s \int_{walls} \vec{H}_c \cdot \vec{H}_c dS \quad (C7)$$

By using the same argument that was used in developing (B4), the integrand of the first term on the right can be expressed as

$$(\vec{E}_c \times \vec{H}_b) \cdot \hat{n} = (\vec{E}_c \times \vec{H}_c) \cdot \hat{n} \quad (C8)$$

Substitution of (C7) and (C8) into (42a) and (42b) then yields (25).

ACKNOWLEDGMENT

REFERENCES

1. M. L. Burrows. *A Theory of Eddy-Current Flaw Detection*, Ph.D. dissertation, University of Michigan, Ann Arbor, MI (1964).
2. D. M. Pozar. *Microwave Engineering*, Addison–Wesley, Reading, MA (1990).
3. R. E. Collin. *Foundations for Microwave Engineering*, 2nd ed., McGraw–Hill, New York (1992).
4. H. L. Libby. *Introduction to Electromagnetic Nondestructive Test Methods*, Wiley–Interscience, New York (1971).
5. A. J. Bahr. In *Eddy-Current Characterization of Materials and Structures*, ASTM STP 722, G. Birnbaum and G. Free, eds. (1981), pp. 332–347.
6. B. A. Auld. In *Eddy-Current Characterization of Materials and Structures*, ASTM STP 722, G. Birnbaum and G. Free, eds. (1981), pp. 332–347.
7. A. J. M. Zaman, C. G. Gardner, and S. A. Long. *J. Nondestr. Eval.* **3**:37–43 (1982).
8. R. F. Harrington. *Time Harmonic Electromagnetic Fields*, McGraw–Hill, New York (1961).
9. S. K. Burke. *J. Phys. D Appl. Phys.* **19**:1159–1173 (1986).
10. J. R. Bowler. *J. Appl. Phys.* **61**:833–839 (1987).
11. J. R. Bowler, L. D. Sabbagh, and H. A. Sabbagh. *IEEE Trans. Magnet.* **25**:2650–2664 (1989).
12. H. A. Sabbagh, J. R. Bowler, and L. D. Sabbagh. *Nondestr. Test. Eval.* **5**:67–79 (1989).
13. J. Zhou, R. Collins, and D. H. Michael. *Rev. Prog. QNDE* **13A**:295–342 (1994).
14. J. M. Prince, B. P. Hildebrand, and G. L. Hower. *J. Nondestr. Eval.* **12**:209–217 (1993).
15. J. C. Moulder, P. J. Shull, and T. E. Capobianco. *Rev. Prog. QNDE* **6**:601–610 (1987).
16. J. C. Moulder, N. Nakagawa, and P. J. Shull. *Rev. Prog. QNDE* **7A**:147–155 (1988).
17. A. J. M. Zaman, S. A. Long, and C. G. Gardner. *IEEE Trans. Instr. Measure.* **30**:41–45.
18. N. Ida. *Rev. Prog. QNDE* **3A**:547–554 (1984).
19. C. Yeh and R. Zoughi. *Res. Nondestr. Eval.* **6**:35–55 (1994).
20. B. A. Auld, J. C. Moulder, S. Jeffries, P. J. Shull, S. Ayter, and J. Kenney. *Res. Nondestr. Eval.* **1**:1–11 (1989).
21. Y. Sun, H. Lin, Y. K. Shin, Z. You, S. Nath, and W. Lord. *Rev. Prog. QNDE* **9A**:319–326 (1990).
22. D. L. Atherton, W. Curza, T. R. Schmidt, S. Sullivan, and C. Toal. *J. Nondestr. Eval.* **8**:37–43 (1989).
23. D. L. Atherton and W. Curza. *Res. Nondestr. Eval.* **5**:123–134 (1993).
24. K. P. Dharmasena and H. N. G. Wadley. *Rev. Prog. QNDE* **10A**:1111–1118 (1991).
25. H. N. G. Wadley, K. P. Dharmasena, and H. S. Goldberg. *Rev. Prog. QNDE* **10B**:1159–1166 (1991).
26. H. N. G. Wadley, A. H. Kahn, Y. Gefen, and M. Mester. *Rev. Prog. QNDE* **7B**:1589–1598 (1988).
27. H. M. Lewis, I. H. Michael, M. C. Lugg, and R. Collins. *J. Appl. Phys.* **64**:3777–3783 (1988).
28. D. H. Michael, A. M. Lewis, M. McIver, and R. Collins. *Proc. Roy. Soc. London* **A434**:587–603 (1991).
29. R. E. Beissner, M. J. Sablik, and C. M. Teller. *Rev. Prog. QNDE* **2B**:1237–1254 (1983).
30. R. E. Beissner and M. J. Sablik. *Rev. Prog. QNDE* **3A**:633–641 (1984).
31. M. Mayos and J. L. Muller. *J. Nondestr. Eval.* **6**:109–116 (1987).
32. G. L. Burkhardt, E. A. Creek, and J. L. Fisher. *Rev. Prog. QNDE* **13A**:343–356 (1994).
33. B. Wincheski, J. Fulton, and S. Nath. *Rev. Prog. QNDE* **13B**:1939–1946 (1994).
34. W. Sheppard, D. Mih, and K. Tam. *Rev. Prog. QNDE* **1**:395–398 (1982).
35. B. A. Auld. *Rev. Prog. QNDE* **10A**:951–955 (1991).

36. M. Uesaka, T. Nakanishi, and K. Miya. *Rev. Prog. QNDE* **13A**:327–334 (1994).
37. M. Gramz and T. Stepinski. *Res. Nondestr. Eval.* **6**:157–174 (1994).
38. M. Uesaka, T. Nakanishi, K. Miya, H. Komatsu, K. Aoki, and K. Kasai. *IEEE Trans. Magnet.* **31**:870–876 (1995).
39. C. V. Dodd and W. E. Deeds. *J. Appl. Phys.* **39**:2829–2838 (1968).
40. C. V. Dodd, C. C. Cheng, and W. E. Deeds. *J. Appl. Phys.* **45**:638–647 (1974).
41. C. V. Dodd, W. E. Deeds, and J. W. Luguire. *Int. J. NDE* **1**:29–90 (1969).
42. P. Stucky and W. Lord. *Rev. Prog. QNDE* **11A**:299–306 (1990).
43. W. Lord. *Electromagnetic Methods of Nondestructive Testing*, Gordon and Breach, London (1985).
44. A. Krawczyk and J. A. Tegopoulos. *Numerical Modeling of Eddy Currents*, Clarendon, Oxford (1985).
45. S. Nath. *Finite Element and Boundary Element Analysis of Electromagnetic NDE Phenomena*, Ph.D. thesis, EE and Computer Engineering, Iowa State University (1992).
46. R. E. Beissner, *J. Appl. Phys.* **60**:352–356 (1986).
47. N. Nakagawa. *Rev. Prog. QNDE* **10A**:249–254 (1991).
48. Y. Liu, N. Nakagawa, and F. Rizzo. *Rev. Prog. QNDE* **12A**:235–242 (1993).
49. K. Murphy and H. A. Sabbagh. *Rev. Prog. QNDE* **14A**:267–274 (1995).
50. I. Elshafiey, L. Udpa, and S. S. Udpa. *IEEE Trans. Magnet.* **30**:3160–3163 (1994).
51. R. Beissner, G. L. Burkhardt, J. L. Fisher, and T. Kikuta. *Rev. Prog. QNDE* **13A**:273–278 (1994).
52. J. C. Moulder and N. Nakagawa. *Rev. Nondestr. Eval.* **4**:221–236 (1992).
53. N. Nakagawa and J. C. Moulder. *Rev. Prog. QNDE* **13A**:295–301 (1994).
54. E. Uzal, J. C. Moulder, S. Mitra, and J. H. Rose. *J. Appl. Phys.* **74**:2076–2089 (1993).
55. R. Palanisamy, R. B. Thompson, and D. O. Thompson. *Rev. Prog. QNDE* **3A**:569–577 (1984).
56. P. C. French and L. J. Bond. *J. Nondestr. Eval.* **7**:55–69 (1988).
57. D. J. Lynch, A. Mahmood, L. D. Philipp, and O. H. Nguyen. *Res. Nondestr. Eval.* **3**:221–234 (1991).
58. W. S. Dunbar. *J. Nondestr. Eval.* **7**:34–54 (1988).
59. D. McA. McKirdy. *J. Nondestr. Eval.* **8**:45–52 (1989).
60. R. E. Beissner. *J. Nondestr. Eval.* **13**:175–183 (1994).
61. J. R. Bowler, S. A. Jenkins, L. D. Sabbagh, and H. A. Sabbagh. *J. Appl. Phys.* **70**:1107–1114 (1991).
62. R. E. Beissner. *J. Appl. Phys.* **60**:352–356 (1986).
63. A. H. Kahn. *J. Nondestr. Eval.* **7**:3–14 (1988).
64. R. E. Beissner. *J. Nondestr. Eval.* **7**:15–24 (1988).
65. N. Nakagawa. *Rev. Prog. QNDE* **10A**:249–254 (1991).
66. N. Nakagawa, S. Mitra, and J. C. Moulder. *Rev. Prog. QNDE* **11A**:233–240 (1992).
67. N. Nakagawa and J. C. Moulder. *Rev. Prog. QNDE* **12A**:259–263 (1993).
68. Y. Liu, N. Nakagawa, and F. Rizzo. *Rev. Prog. QNDE* **12A**:235–242 (1993).
69. J. R. Bowler. *J. Appl. Phys.* **75**:8128–8137 (1994).
70. C. Kittel. *Introduction to Solid State Physics*, Wiley, New York (1971), pp. 450–454.
71. J. A. Osborne. *Phys. Rev.* **67**:351–357 (1945).
72. S. M. Nair and J. H. Rose. *J. Appl. Phys.* **70**:1924–1937 (1991).
73. G. L. Hower. *J. Nondestr. Eval.* **6**:177–180 (1987).
74. G. L. Hower and D. E. Hadlock. *J. Nondestr. Eval.* **8**:247–255 (1989).
75. D. E. Hadlock and G. L. Hower. *Res. Nondestr. Eval.* **2**:255–237 (1990).
76. A. H. Kahn, R. Spal, and A. Feldman. *J. Appl. Phys.* **48**:4454–4459 (1977).
77. D. T. Paris and F. K. Hurd. *Basic Electromagnetic Theory*, McGraw–Hill, New York (1969), pp. 516–519.

78. W. D. Dover, F. D. W. Charlsworth, K. A. Taylor, R. Collins, and D. H. Michael. In *Eddy Current Characterization of Metals and Structures*, ASTM STP 722, G. Birnbaum and G. Free, eds. (1981), pp. 401–427.

79. R. E. Beissner and M. J. Sablik. *J. Appl. Phys.* **56**:448–454 (1984).

80. B. A. Auld, G. McFettridge, M. Riaziat, and S. Jefferies. *Rev. Prog. QNDE* **4A**:623–634 (1985).

81. N. Nakagawa, J. Chao, and A. N. S. Prasad. In *Nondestructive Testing of Materials*, R. Collins et al., eds., IOS Press, London (1996), p. 203.

82. N. Nakagawa and J. Chao. *Rev: Prog. QNDE* **15A**:339–345 (1996).

83. J. Chao, D. Lether, J. C. Moulder, and N. Nakagawa. *Rev. Prog. QNDE* **15A**:355–360 (1996).

84. B. A. Auld, F. Muennemann, and D. K. Winslow. *J. Nondestr. Eval.* **2**:1–21 (1981).

85. B. A. Auld, F. G. Muennemann, and M. Riaziat. In *Nondestructive Testing 7*, R. S. Sharpe, ed., Academic Press, London, (1984), pp. 38–75.

86. S. K. Burke. *J. Nondestr. Eval.* **7**:35–44 (1988).

87. R. E. Beissner. *J. Nondestr. Eval.* **7**:25–34 (1988).

88. N. Harfield and J. R. Bowler. *J. Appl. Phys.* **76**:4853–4856 (1994).

89. G. L. Hower and R. W. Rupe. *J. Nondestr. Eval.* **4**:59–63 (1984).

90. D. H. Michael, R. Collins, D. R. Parramore, M. Aldoujailly, and P. R. Travis. *Rev. Prog. QNDE* **7A**:191–197 (1988).

91. B. A. Auld, S. R. Jefferies, and J. C. Moulder. *J. Nondestr. Eval.* **7**:79–84 (1988).

92. T. Takagi, M. Hashimoto, T. Jugiura, S. Norimatsu, S. Arita, and K. Miya. *Rev. Prog. QNDE* **9A**:327–334 (1990).

93. Z. Badics, H. Komatsu, H. Motosuji, K. Aoki, and F. Nakayasu. *Int. J. Electromag. Mater.* **4**:357–362 (1994).

94. Z. Badics, Y. Matsumoto, K. Aoki, F. Nakayasu, M. Uesaka, and K. Miya. *J. Nondestr. Eval.* **14**:181–192 (1995).

95. J. R. Bowler. *Electrosoft* **2**:142–156 (1991).

96. R. E. Beissner. *Electrosoft* **2**:122–141 (1991).

97. D. Lether, J. Chao, N. Nakagawa, and J. C. Moulder. *Rev. Prog. QNDE* **15A**:361–368 (1996).

98. M. Riaziat and B. A. Auld. *Rev. Prog. QNDE* **3A**:511–521 (1984).

99. M. Riaziat. *Analytic Methods in Electromagnetic Nondestructive Evaluation*, Ph.D. thesis, Department of Electrical Engineering, Stanford University, Stanford, CA (1984).

100. N. Harfield and J. R. Bowler. *Rev. Prog. QNDE* **13A**:279–286 (1994).

101. W. Lord and R. Palanisamy. In *Eddy Current Characterization of Materials and Structures*, ASTM STP 722, G. Birnbaum and G. Free, eds. (1981), pp. 5–21.

102. J. C. Treece, K. Murphy, and H. A. Sabbagh. *Rev. Prog. QNDE* **13A**:319–326 (1994).

103. B. A. Auld and M. Riaziat. *J. Appl. Phys.* **54**:3509–3517 (1983).

104. R. Collins, D. Mirshekar-Syakahl, and D. H. Michael. *Proc. Roy. Soc. London* **A393**:159–170 (1984).

105. D. McA. McKirdy. *Rev. Prog. QNDE* **12A**:265–270 (1993).

106. N. Ida, H. Hoshikawa, and W. Lord. *NDE Int.* **18**:331–338 (1985).

107. S. J. Norton, A. H. Kahn, and M. L. Mester. *Res. Nondestr. Eval.* **1**:167–179 (1989).

108. J. H. Rose, E. Uzal, and J. C. Moulder. *SPIE* **2160**:164–175 (1994).

109. B. A. Auld, J. Kenney, and T. J. Lookabaugh. *Rev. Prog. QNDE* **5A**:681–690 (1986).

110. A. J. Bahr. *Rev. Prog. QNDE* **5A**:691–698 (1986).

111. A. Rosengreen, A. J. Bahr, and D. M. Marsland. *Rev. Prog. QNDE* **7A**:493–500 (1988).

112. C. V. Dodd and W. E. Deeds. *Rev. Prog. QNDE* **1**:387–394 (1982).

113. M. Riaziat and B. A. Auld. *Rev. Prog. QNDE* **2A**:189–204 (1983).

114. A. J. Bahr and D. W. Cooley. *Rev. Prog. QNDE* **2A**:225–244 (1983).

115. J. J. Brandstatter. *An Introduction to Waves, Rays, and Radiation in Plasma Media*, McGraw-Hill, New York (1963).

116. D. C. Copley. *Rev. Prog. QNDE* **2B**:1527–1540 (1983).

117. P. M. Morse and H. Feshbach. *Methods of Theoretical Physics*, Wiley, New York (1953), Part I, pp. 137–138.

118. J. H. Hippler, H. Emert, and L. von Bernus. *J. Nondestr. Eval.* **12**:153–162 (1993).

119. J. M. Prince, B. P. Hildebrand, and G. L. Hower. *J. Nondestr. Eval.* **12**:209–217 (1993).

120. H. D. Collins, T. J. Davis, and L. J. Busse. *Acoust. Imaging* **11**:37–43 (1982).

121. S. M. Nair and J. H. Rose. *Inverse Problems* **6**:1007–1030 (1990).

122. J. H. Rose and S. M. Nair. *Inverse Problems* **7**:131–136 (1991).

123. A. J. Bahr and B. A. Auld. *J. Nondestr. Eval.* **7**:71–77 (1988).

124. B. R. Groshong, G. L. Bilbro, and W. E. Synder. *J. Nondestr. Eval.* **10**:127–137 (1991).

125. L. D. Sabbagh and H. A. Sabbagh. *Rev. Prog. QNDE* **2B**:155–157 (1983).

126. L. D. Sabbagh and H. A. Sabbagh. *Rev. Prog. QNDE* **4A**:635–643 (1985).

127. L. Udpa and S. S. Udpa. *J. Nondestr. Eval.* **7**:111–120 (1988).

128. M. P. Connolly, D. H. Michael, and R. Collins. *J. Appl. Phys.* **64**:2638–2647 (1988).

129. S. J. Norton and J. R. Bowler. *J. Appl. Phys.* **73**:501–512 (1993).

130. J. R. Bowler, S. J. Norton, and D. J. Harrison. *J. Appl. Phys.* **75**:8138–8144 (1994).

131. S. K. Burke. *J. Appl. Phys.* **76**:3072–3080 (1994).

132. B. A. Auld, S. Jefferies, J. C. Moulder, and J. C. Gerlitz. *Rev. Prog. QNDE* **5A**:383–393 (1986).

133. J. C. Moulder, E. Uzal, and J. H. Rose. *Rev. Sci. Instrum.* **63**:3455–3465 (1992).

134. E. Uzal, J. C. Moulder, S. Mitra, and J. H. Rose. *J. Appl. Phys.* **74**:2076–2089 (1993).

135. A. Sethuraman and J. H. Rose. *J. Nondestr. Eval.* **14**:39–46 (1995).

136. J. H. Rose, E. Uzal, and J. C. Moulder. *SPIE* **2160**:164–176 (1994).

137. D. J. Harrison, L. D. Jones, and S. K. Burke. *J. Nondestr. Eval.* **15**:21–34 (1996).

138. R. E. Beissner, M. J. Sablik, K. J. Krzywosz, and J. E. Doherty. *Rev. Prog. QNDE* **2B**:1159–1286 (1983).

139. R. E. Beissner and J. L. Fisher. *Rev. Prog. QNDE* **5A**:189–197 (1985).